HHS Public Access

Author manuscript

Cell. Author manuscript; available in PMC 2021 May 10.

Published in final edited form as:

Cell. 2018 May 03; 173(4): 972–988.e23. doi:10.1016/j.cell.2018.03.050.

DNA Repair Network Analysis Reveals Shieldin as a Key Regulator of NHEJ and PARP Inhibitor Sensitivity

Rajat Gupta[1], **Kumar Somyajit**[2], **Takeo Narita**[1], **Elina Maskey**[1], **Andre Stanlie**[3], **Magdalena Kremer**[4], **Dimitris Typas**[2], **Michael Lammers**[4,5], **Niels Mailand**[2], **Andre Nussenzweig**[3], **Jiri Lukas**[2], **Chunaram Choudhary**[1,6,7,*]

[1]Proteomics Program, the Novo Nordisk Foundation Center for Protein Research, Faculty of Health and Medical Sciences, University of Copenhagen, Blegdamsvej 3B, DK-2200 Copenhagen, Denmark

[2]Protein Signaling Program, the Novo Nordisk Foundation Center for Protein Research, Faculty of Health and Medical Sciences, University of Copenhagen, Blegdamsvej 3B, DK-2200 Copenhagen, Denmark

[3]Laboratory of Genome Integrity, NIH, Bethesda, MD 20892, USA

[4]Institute for Genetics and Cologne Excellence Cluster on Cellular Stress Responses in Aging-Associated Diseases (CECAD), Joseph-Stelzmann-Str. 26, University of Cologne, 50931 Cologne, Germany

[5]Institute for Biochemistry, Synthetic and Structural Biochemistry, Felix-Hausdorff-Str. 4, University of Greifswald, 17487 Greifswald, Germany

[6]Center for Chromosome Stability (CCS), Faculty of Health and Medical Sciences, University of Copenhagen, Blegdamsvej 3B, DK-2200 Copenhagen, Denmark

[7]Lead Contact

SUMMARY

Repair of damaged DNA is essential for maintaining genome integrity and for preventing genome-instability-associated diseases, such as cancer. By combining proximity labeling with quantitative mass spectrometry, we generated high-resolution interaction neighborhood maps of the endogenously expressed DNA repair factors 53BP1, BRCA1, and MDC1. Our spatially resolved interaction maps reveal rich network intricacies, identify shared and bait-spe-cific interaction

*Correspondence: chuna.choudhary@cpr.ku.dk.

AUTHOR CONTRIBUTIONS

R.G. designed all plasmid constructs, generated all genetically modified cell lines used in this study, and performed all proteomic experiments. K.S. and R.G. designed and performed functional assays, analyzed the data, and prepared figures. T.N. analyzed data, constructed the *de novo* networks, and prepared figures. E.M. provided expert technical assistance. N.M. and D.T. provided the RINN1 antibody. A.S. and A.N. performed antibody CSR and metaphase spread analyses. M.L. and M.K. purified recombinant RINN1 and REV7 and measured their interaction *in vitro*. J.L. supervised K.S., designed experiments, and analyzed the data. C.C. and R.G. conceived the project and wrote the manuscript. All authors read and commented on the manuscript.

SUPPLEMENTAL INFORMATION

Supplemental Information includes seven figures and seven tables and can be found with this article online at https://doi.org/10.1016/j.cell.2018.03.050.

DECLARATION OF INTERESTS

The authors have no conflict of interest to declare.

modules, and implicate previously concealed regulators in this process. We identified a novel vertebrate-specific protein complex, shieldin, comprising REV7 plus three previously uncharacterized proteins, RINN1 (CTC-534A2.2), RINN2 (FAM35A), and RINN3 (C20ORF196). Recruitment of shieldin to DSBs, via the ATM-RNF8-RNF168–53BP1-RIF1 axis, promotes NHEJ-dependent repair of intrachromosomal breaks, immunoglobulin class-switch recombination (CSR), and fusion of unpro-tected telomeres. Shieldin functions as a downstream effector of 53BP1-RIF1 in restraining DNA end resec-tion and in sensitizing *BRCA1*-deficient cells to PARP inhibitors. These findings have implications for under-standing cancer-associated PARPi resistance and the evolution of antibody CSR in higher vertebrates.

INTRODUCTION

DNA damage presents a major threat to genome stability, and cells have therefore evolved elegant mechanisms, collectively referred to as the DNA damage response (DDR), to protect their genome integrity (Jackson and Bartek, 2009). Among different types of damage, DNA double-strand breaks (DSBs) are one of the most severe types of DNA lesions. DSBs are repaired through two major pathways: homology-directed repair (HDR) and non-homologous end joining (NHEJ) (Ceccaldi et al., 2016). The tumor suppressor 53BP1 plays an important role in DSB repair pathway choice and in enhancing the fidelity of DSB repair. In G1, 53BP1 promotes classical NHEJ over more error-prone alternative end joining (Ceccaldi et al., 2016; Chapman et al., 2013; Escribano-Díaz et al., 2013); in S/G2, it guards DSB against hyper-resection to restrain mutagenic forms of HDR, such as single-strand annealing (Ochs et al., 2016). RIF1 is the most proximal effector of 53BP1 in its anti-resection function, and recent work identified REV7 as a downstream factor in 53BP1-/RIF1-dependent DSB repair pathway choice (Boersma et al., 2015; Xu et al., 2015).

In the physiological context, the 53BP1/RIF1/REV7 pathway promotes NHEJ, telomere maintenance, and immunoglobulin class-switch recombination (CSR). In the clinical context, cells lacking key HDR regulators, such the tumor suppressor BRCA1, are hyper-sensitive to PARP inhibitors (PARPi) (Bryant et al., 2005; Farmer et al., 2005). Three different PARPi (olaparib, rucaparib, and niraparib) were recently approved for the treatment of HDR-defective cancers (Lord and Ashworth, 2017). Remarkably, genetic depletion of *53BP1*, *RIF1*, or *REV7* provides synthetic viability to *BRCA1*-deficient cells and affords resistance to PARPi in HDR-defective cells (Boersma et al., 2015; Bunting et al., 2010; Lord and Ashworth, 2017; Xu et al., 2015).

Despite their important roles in DSB repair, 53BP1, RIF1, and REV7 contain no known enzymatic activity, no direct interactions are shown between them, and the identity of downstream effector(s) in this pathway is unknown. Identification of 53BP1 downstream effector(s) is crucial for understanding the cellular pathways and molecular mechanisms of DSB repair. A major challenge in investigating DDR networks is that isolation of the “DDR factories” is intractable to most biochemical methods, and the high-stringency conditions required for extracting chromatin-bound complexes are incompatible with preserving physiologically relevant protein-protein interactions.

To circumvent these limitations and to provide a holistic view of the "DSB repairosome," we combined CRISPR-based genome editing (Cong et al., 2013), APEX-based proximity labeling (Rhee et al., 2013), and quantitative mass spectrometry (MS) to survey protein networks in the neighborhood of the endogenously expressed DDR factors 53BP1, BRCA1, and MDC1. This allowed us to map their interaction landscape in the native environment, revealing new insights into the global DDR networks. Notably, we discovered a vertebrate-specific novel protein complex, shieldin, which functions as a downstream effector in the 53BP1 pathway, regulates NHEJ in various settings, and impacts resistance to PARPi in HDR-defective cells. These findings have implications for understanding the evolution of antibody diversification, as well as for understanding the mechanisms of PARPi-resistance with possible clinical ramifications.

RESULTS

APEX Tagging of the Endogenous DDR Factors

We used CRISPR-Cas9-based genome editing to fuse a 3×-FLAG-affinity tag and *APEX2* (hereafter APEX) at the N terminus of the endogenous *53BP1*, *BRCA1*, and *MDC1* in U2OS cells (Figure 1A). The FLAG tag was included for affinity purification and MS (AP-MS) of the bait proteins, and APEX was included for *in vivo* biotinylation-based analysis of bait-proximal networks (hereafter PROX-NET). Correctly modified cell clones were identified by genomic PCR and immunoblotting (Figures 1B and S1A), and competent localization of the bait proteins to DSBs was confirmed by analyzing their localization to ionization radiation-induced foci (IRIF) (Figure S1B). The functionality of APEX was confirmed by selective biotinylation in the engineered cells (Figure 1C).

Strategy for Mapping the Endogenous DDR Networks

For PROX-NET analyses, bait-proximal proteins were biotinylated by treating the cells with H_2O_2 for 2 min. Non-nuclear proteins were removed by subcellular fractionation, and nuclear lysates from APEX-bait-expressing cells and control cells were mixed prior to enrichment of biotinylated proteins. The affinity-enriched proteins were quantified with stable isotope-based labeling in cell culture (SILAC)-based MS (Figure 1D).

Even though a low level of DNA damage occurs under normal physiological settings, DDR signaling is often studied using exogenous DNA-damaging agents. In our initial PROX-NET analyses, we compared interaction networks with and without ionization radiation. Surprisingly, the efficiency of APEX-induced biotinylation was reduced after ionization radiation (IR)-induced DNA damage (Figures S1C and S1D; Table S1), resulting in decreased enrichment of the bait itself, as well as of bait-associated known DDR factors. Therefore, all subsequent PROX-NET analyses presented here were performed in exponentially growing cells without exogenous DNA damage. This was not a disadvantage —on the contrary, by this approach, we came closer to physiological settings by assessing the DSB landscape at stochastic, low-abundant lesions that did not saturate rate-limiting factors (Toledo et al., 2013). We performed six replicates for each bait and identified a total of >3,500 proteins (Table S2). Notably, known DDR factors showed significantly higher SILAC ratios and were effectively separated from non-DDR proteins (Figure 1E).

To identify bait-proximal networks, significantly enriched proteins were defined as having ≥2-fold mean enrichment in the APEX-engineered cells compared to control cells and quantified in at least two independent biological replicates. Using these parameters, we filtered out 89% of the identified proteins as unspecific "background binders," leaving ~400 proteins that were considered bait-specific network interactors (Table S3), three-quarters of which were quantified in ≥3 independent replicates (Figure S1E). While a majority (>58%) of the background binders were enriched commonly in all baits, just 3.6% of the significantly enriched proteins were commonly detected in all three baits (Figure 1F). These results show that despite common involvement of 53BP1, BRCA1, and MDC1 in the DDR, their interaction profiles are sufficiently distinct to allow differentiating specific interactors from a large number of background binders.

To directly compare the performance of PROX-NET with the traditional AP-MS approach, we affinity enriched the endogenously expressed baits using anti-FLAG antibodies, and interacting proteins were quantified by SILAC. PROX-NET analyses identified many more interactors compared to the AP-MS method (Figure S1F). Also, a comparison of the PROX-NET dataset with the cumulated AP-MS-based interactions from the BioGRID database (Chatr-Aryamontri et al., 2017) showed that PROX-NET analyses identified ~3.5 times more known DDR factors as compared to AP-MS (Figure S1G). These results show that, in addition to identifying core interactors, PROX-NET analyses captured extended bait-interaction networks. We classify PROX-NET-based interactions as "neighborhood interactions" to distinguish them from AP-MS-based interactions that mostly include direct protein-protein interactions.

Bait-Specific Enrichment of DDR and Non-DDR Pathways

The 53BP1 network encompassed the greatest number of neighborhood interactors, followed by BRCA1 and MDC1 (Figure 1G). Overall, ~40% of proteins from the PROX-NET dataset have previously been implicated in DNA damage repair, DNA replication, or telomere maintenance (hereafter referred to as "DDR factors") (Table S3). Among the top 100 highly enriched proteins for each bait, over half have previously been implicated in the DDR (Figure 2A), independently validating the quality of our dataset. Because not all proteins involved in the DDR are known, and our reference curation is likely incomplete, the actual fraction of DDR-related proteins in our dataset is likely underestimated. For example, RAD54L2 and SLX4IP interact with known DDR factors, but their role in the DDR has not been reported, and therefore, in our dataset, they were not included among known DDR factors.

Consistent with the involvement of the bait proteins in the DDR, Gene Ontology (GO) terms, such as "DNA repair," "telomere maintenance," and "double-strand break repair by HDR and NHEJ," were significantly overrepresented with all three baits (Figure S1H). GO terms such as "inter-strand cross-link repair," "base excision repair," and "mismatch repair" were more significantly or exclusively enriched with BRCA1, whereas the terms "histone acetylation," "protein ubiquitylation," and "protein sumoylation" were more prominently enriched with 53BP1. In particular, many proteins involved in sumoylation, including

SUMO1, SUMO2/SUMO3, UBE2I, PIAS1/PIAS2, PIAS3, and ZNF451 were enriched with 53BP1.

In addition to DDR factors, several non-DDR proteins showed bait-specific enrichment in our dataset (Figure S2A). This is consistent with a close connection between gene transcription and the DDR (Gaillard and Aguilera, 2016), as well as with the reported functions of the bait proteins in non-DDR processes. For example, many transcriptional regulators were enriched in the 53BP1-proximal networks, consistent with low-affinity, DNA damage-independent interaction of 53BP1with chromatin (Bekker-Jensen et al., 2005; Difilippantonio et al., 2008). Also, several centromere- and kinetochore-associated proteins were enriched with BRCA1, which is consistent with the localization of BRCA1 to these structures (Pageau and Lawrence, 2006) and with the reported role of centromeric BRCA1 in preventing chromosome missegregation (Di Paolo et al., 2014). Together, our results support shared and distinct functional networks of 53BP1, BRCA1, and MDC1 in diverse DDR and non-DDR-associated processes.

PROX-NET-Based Map of the DDR Networks

Our PROX-NET dataset included >170 known DDR factors, many of which are not reported to interact directly with the bait proteins, and their relative enrichment near the baits is not known. Mapping of our quantitative data to known pathways and protein complexes revealed several interesting insights. First, individual components of protein complexes showed highly consistent, bait-specific enrichment (Figure 2B). For example, subunits of the MRN complex were enriched with all three baits, whereas members of the 9-1-1 complex were enriched in the 53BP1 and BRCA1 neighborhoods only. Second, different protein complexes showed different degrees of enrichment. For instance, the MRN complex was enriched more strongly with all three baits as compared to the SWI/SNF complex. Third, proteins defining unique complexes were distinguishable from proteins that are shared between different complexes. For example, from the three different BRCA1 complexes (Savage and Harkin, 2015), the BRCA1 B and C complexes, defined by BACH1 and CTIP, respectively, were exclusively enriched with BRCA1, whereas members of the BRCA1 A complex were enriched with all three baits. Finally, subcomplexes within larger protein assemblies could be delineated. For example, from the SLX4-ERCC4 (XPF)-ERCC1, MUS81-EME1 “supercomplex” (Wyatt et al., 2017), we could distinguish the dynamic MUS81-EME1 and XPF-ERCC1 subcomplexes (Figure 2B). Similarly, distinct enrichment patterns suggest that SLF1-SLF2 forms a subcomplex within the RAD18-SLF1-SLF2-SMC5/6 supercomplex (Räschle et al., 2015). These results demonstrate that, in addition to identifying direct interactors, the PROX-NET approach is highly efficient in capturing many additional bait-proximal complexes, and the quantitative profiles can inform about dynamic subcomplexes that may constitute hitherto unrecognized functional modules.

In addition to DSB repair, our analyses captured major regulators of telomere-associated processes, such as end protection (the shelterin complex) (Palm and de Lange, 2008), termination of telomerase activity and telomere protection (the CST complex) (Chen et al., 2012), coupling of telomere replication and end protection (hnRNPA1 and A2/B1) (Flynn et al., 2011), telomere trimming (TZAP) (Li et al., 2017), overhang processing (Apollo/

DCLRE1B) (Wu et al., 2012), lagging-strand synthesis (WRN) (Crabbe et al., 2004), and other aspects of telomere maintenance (HOT1, ZNF827) (Conomos et al., 2014; Kappei et al., 2013) (Figures S2B and S2C). Notably, HOT1, TZAP, ZNF827, WRN, and the CST complex showed a distinct bait-specific enrichment pattern (characterized by their lack of enrichment with MDC1) compared to shelterin and hnRNPs, suggesting their spatial segregation. Notably, most of these telomere-maintenance proteins co-localize with shelterin microscopically, yet the PROX-NET data unambiguously reveal their spatial separation, showing the outstanding resolution of our dataset and illustrating how these quantitative networks can be mined to further subclassify well-studied protein complexes and pathways.

Next, we asked whether PROX-NET-based quantitative interaction profiles could be used to obtain a *de novo* picture of the neighborhood interaction networks. We used SILAC ratios of interactors, their bait-specificity, and enrichment frequency in replicate experiments to calculate pairwise correlation for all proteins that were enriched in our dataset and used these data to generate *de novo* interaction networks (Figure S3). These networks faithfully recapitulated many known binary interactions and protein complexes, including the BRCA1 A, MRN, CFIm, and shelterin, highlighting the potential of our approach in constructing *de novo* interaction networks.

Identification of RINN1

To further demonstrate the potential of our datasets in identifying novel components of the DDR, we were intrigued to find a novel 250-amino-acid protein (CTC-534A2.2; UniProt: Q6ZNX1) that was among the top hits that was reproducibly enriched in proximity to 53BP1, but not with BRCA1 or MDC1 (Figure 3A). In our *de novo* networks, it was predicted to interact with proteins including USP28 and REV7, which function with 53BP1 in the DSB repair (Boersma et al., 2015; Xu et al., 2015). We named this novel protein as RINN1 (REV7-interacting novel NHEJ regulator 1) based on its function that will become apparent later. *RINN1* is encoded by a single exon, and the gene is nested within the first intron of *TRAPPC13* (Figure S4A). We generated a RINN1 antibody (Figure S4B) and confirmed RINN1 expression in diverse human cell lines (Figure S4C).

RINN1 Directly Interacts with REV7

To identify its function, we performed label-free AP-MS analyses of RINN1 and identified REV7 as an interactor; conversely, RINN1 was enriched in REV7 pull-downs (Table S4). RINN1 and REV7 interacted reciprocally, the interaction was unaffected by DNA damage, and the interaction region was mapped to amino acids 28–83 in RINN1 (Figures 3B and 3C). Recombinant $RINN1_{28–83}$ and REV7 formed a complex *in vitro* (Figure 3D), and the interaction affinity was measured to be ~15 nM, demonstrating a direct interaction between these proteins (Figures 3E and S4D). Sequence alignment of the REV7-interacting region in RINN1 revealed four residues (F38, W41, P53, and P58) that are invariably conserved in diverse species (Figure S4E). Mutation of bulky Trp and Phe could affect the overall protein structure; therefore, we mutated the conserved proline residues, which are mostly found in loops and thus are less likely to impact the overall protein structure. Notably, the mutant $RINN1_{P53A,P58A}$ was completely deficient for interaction with REV7 (Figure 3F).

RINN1 Functions Downstream of 53BP1-RIF1

Based on its novelty and strong interaction with REV7, we investigated the function of RINN1 in DSB repair. We found that RINN1 dose-dependently accumulated at IRIF, where it colocalized with γH2AX and REV7, as well as with 53BP1 and RIF1 (Figures 4A and 4B). DSB recruitment of RINN1 required the ataxia-telangiectasia-mutated (ATM) kinase activity, as well as RNF8-RNF168-dependent recruitment of 53BP1 and RIF1 (Figure 4C and S5A), whereas RIF1 was recruited independent of RINN1 (Figure S5B). REV7 and PTIP were dispensable for RINN1 recruitment, whereas RINN1 was required for REV7 recruitment (Figures 4C, S5C, and S5D), placing RINN1 function upstream of REV7 in this pathway. Consistently, RINN1 wild-type, but not $RINN1_{P53A,P58A}$, rescued REV7 recruitment in *RINN1*-depleted cells (Figure 4D). Collectively, these results show that RINN1 is recruited to DSBs via the ATM-RNF8-RNF168–53BP1-RIF1 axis (Figure 4E), establishing RINN1 as a potential link between the proximal 53BP1-RIF1 module and its downstream effector(s) in DSB repair.

RINN1 Recruitment to DSB Sites Is Cell-Cycle Regulated

RIF1 binding to 53BP1 is regulated during the cell cycle—being high in G1 and gradually attenuating during switch (S) phase (Chapman et al., 2013; Escribano-Díaz et al., 2013). In a striking similarity, we found that RINN1 IRIF were primarily restricted to cells in G1/early S, and the number of foci and their intensity decreased as cells progressed to late S/G2 (Figures 4F and S6A). The differential recruitment of RINN1 was not due to altered protein expression during the cell cycle (Figure S6B). In the fraction of cells that formed RINN1 IRIF in early S phase, RINN1 foci were largely excluded from those decorated by BRCA1 and RAD51, respectively (Figure S6C). This is again reminiscent of RIF1, which forms IRIF in G1 but is opposed by BRCA1 in S/G2 (Chapman et al., 2013; Escribano-Díaz et al., 2013). Consistent with previous reports showing that BRCA1 deficiency restores RIF1 IRIF formation beyond G1 (Escribano-Díaz et al., 2013), depletion of *BRCA1* increased RINN1 recruitment to IRIF and restored RINN1 IRIF formation in S/G2 (Figures 4G and S6D). We conclude that recruitment of RINN1 to DSBs is regulated during the cell cycle and that BRCA1 opposes RINN1 recruitment, possibly by antagonizing RIF1, which, as we show, is required for RINN1 assembly at IRIF.

RINN1 Is a Novel Regulator of NHEJ

DSBs are repaired via the HDR or NHEJ. Given the established role of 53BP1-RIF1-REV7 in DSB repair (Hustedt and Durocher, 2016) and our finding that RINN1 is a component of this pathway, we posited that RINN1 might function in DSB repair. Initially, we used a HDR reporter that scores short-tract gene conversion, but we did not observe a substantial effect of *RINN1* knockdown in this assay (Figure S6E). This is consistent with the recent findings showing that extensive DNA resection of DSB ends, which is progressive and inevitable in cells lacking 53BP1 or any of its downstream components, eventually compromises gene conversion (GC) at the expense of single-stranded DNA, an alternative mode of HDR triggered by DSB hyper-resection (Ochs et al., 2016; Xie et al., 2018). We therefore tested the role of RINN1 in classical NHEJ (cNHEJ), which is strongly influenced by the 53BP1 pathway (Ceccaldi et al., 2016) and where lack of DNA end protection, regardless of its

extent, would have a detrimental effect on the repair outcome. Notably, knockdown of *RINN1* significantly impaired NHEJ (Figures 5A and 5B), and co-depletion of *REV7* did not alter the effect of *RINN1* knockdown in this assay (Figure S6F). The NHEJ defect in *RINN1*-depleted cells could be partially rescued by expressing small interfering RNA (siRNA)-resistant *RINN1* wild-type, but not by $RINN1_{P53A,P58A}$ (Figure S6G), further supporting the notion that RINN1 interaction with REV7 is important for its function in NHEJ.

To further characterize RINN1 function in other NHEJ-dependent processes, we investigated its role in the protection of uncapped telomeres. We used a temperature-sensitive TRF2 mutant (TRF2ts) cell line that grows normally at low temperature (32°C) but shows telomere uncapping and NHEJ-dependent telomere fusion at elevated temperature (39°C) (Boersma et al., 2015; Konishi and de Lange, 2008). Similar to *REV7* knockdown (Boersma et al., 2015) (Figure S6H), depletion of *RINN1* substantially reduced the fusion of uncapped telomeres, and this effect was blunted in cells expressing short hairpin RNA (shRNA)-resistant *RINN1* (Figure 5C). Moreover, phosphorylation of ATM, γH2AX, and CHK1, which indicate activation of DNA damage signaling, was increased in RINN1-depleted cells after telomere uncapping at 39°C (Figure S6I). Together, these results demonstrate a key role of RINN1 in promoting the NHEJ pathway.

Identification of the Shieldin Complex

To further understand the link between RINN1 and the DDR, we performed in-depth RINN1 interaction analyses using SILAC-based AP-MS. These analyses confirmed RINN1 interaction with REV7, but no interaction was detected with 53BP1, RIF1, or other known DSB repair factors. Instead, RINN1 interacted with two completely uncharacterized proteins, FAM35A and C20ORF196 (Figure 5D and Table S5), and FAM35A was also enriched in the 53BP1 PROX-NET dataset (detected in one experiment) (Table S2). Based on their interactions and functional similarity with RINN1 (see below), we named FAM35A as RINN2 and C20orf196 as RINN3 (RINN1-REV7-interacting novel NHEJ-regulator 2 and 3, respectively). A similar abundance of RINN1 and REV7 in the AP-MS data implies that they interact at 1:1 stoichiometry (Figure 5D), whereas a lower abundance of RINN2–3 in these experiments implies a sub-stoichiometric interaction or a weaker interaction affinity.

Interaction between RINN1 and the newly identified components was verified by co-immunoprecipitations (Figure 5E). The interaction of RINN1 with these proteins remained unchanged after IR treatment, indicating that they interact constitutively in a DNA-damage-independent manner. The deletion mutants showed that the N-terminal region of RINN2 interacted with RINN1-REV7 (Figure 5F); further analysis of this region revealed that amino acids 1–60 (named here as RIM motif for RINN1-REV7 interaction motif) of RINN2 was sufficient to interact with RINN1-REV7 (Figure 5G). Indeed, deletion of conserved amino acids 6–11 in the RIM motif completely abolished RINN2 interaction with RINN1-REV7 (Figure 5H). Using a similar domain mapping strategy, we found that the C-terminal FAM35 domain (amino acids 650–835) of RINN2 was required for interaction with RINN3 (Figure 5I). Together, these results show that RINN1–3 and REV7 physically interact to

form a novel protein complex (Figure 5J), which we named shieldin (based on its function in DSB protection and NHEJ, which will become apparent later).

Surprisingly, while the transcripts encoding *RINN1–3* are expressed universally across diverse human tissues (Figure S6J), their protein expression is virtually undetectable in MS-based global proteome analyses. In the UniProt database, RINN1 and RINN3 are annotated as hypothetical proteins based on their mRNA expression. We measured the proteome of U2OS cells to a depth of ~10,000 proteins, which included all proteins that were enriched in our PROX-NET dataset (excepting RHNO1) (Table S6); however, no peptides were detected for RINN1–3. In contrast, these proteins were detected with multiple peptides in the RINN1 AP-MS analyses (Figure 5D), showing that lack of their detection in global proteome datasets is not due to technical reasons, but likely due to their ultra-low abundance in cells.

Shieldin Regulates NHEJ and Antibody CSR

Analysis of RINN2–3 showed that both proteins localize to γH2AX-marked IRIF (Figure 6A). While recruitment of RINN1 to IRIF was not reduced by knockdown of RINN2–3, recruitment of RINN2–3 and REV7 appears to be interdependent (Figure 6B), indicating that they are possibly recruited as a complex. Next, we investigated the function of RINN2–3 in NHEJ. Similar to *RINN1*, depletion of *RINN2–3* markedly reduced NHEJ (Figures 6C and S6K). 53BP1-RIF1-dependent NHEJ is critically important for immunoglobulin CSR (Ward et al., 2004). Therefore, to test the relevance of shieldin in this physiological process, we depleted *Rinn1–3* in CH12 cells, which undergo cytokine-stimulation-dependent CSR *in vitro*. Indeed, knockdown of *Rinn1–3*, as well as genetic knockout of *Rinn1* and *Rinn3*, severely reduced CSR (Figures 6D and S7A), demonstrating a critical role of shieldin in immunoglobulin diversification.

Antibody CSR is widely believed to have evolved recently in amphibians (Chaudhuri et al., 2007); however, recent work showed that nurse sharks show a primordial form of CSR (Zhu et al., 2012). To understand the evolution of DSB repair pathways involved in CSR, we searched orthologs of key genes involved in DSB repair and CSR across diverse eukaryotes. These analyses revealed a recent evolution of RINN1–3 and indicated that RINN3 is the most recently evolved regulator of CSR (Figures 6E and S7B). Together, these results show a modern evolution of the shieldin complex and indicate that shieldin and the CSR mechanism evolved simultaneously.

Shieldin Impacts DNA End Resection

The 53BP1-RIF1-REV7 axis controls DNA end resection (Ceccaldi et al., 2016). Therefore, we investigated the function of newly identified shieldin components in DNA end resection by measuring chromatin binding of RPA, which binds to resected single-stranded DNA and is widely used as a proxy for measuring resected DSBs. *RINN1* knockout (Figure S7C) showed excessive resection as indicated by increased binding of RPA to chromatin (Figure 6F) and enhanced native BrdU staining (Figure 6G). Similarly, knockdown of *RINN1–3* also caused increased loading of RPA to chromatin (Figure 6H). Depletion of *RINN1* increased RAD51 chromatin loading; this effect required CTIP-dependent end resection (Figure S7D); re-introduction of *RINN1* wild-type, but not $RINN1_{P53,P58A}$, rescued RPA and RAD51

staining (Figure S7E). Together, these results show that knockdown of shieldin components results in increased end resection. Because excessive or unscheduled resection would make DNA ends unsuitable for repair by NHEJ (Escribano-Díaz et al., 2013), this may explain defective NHEJ in shieldin-depleted cells.

Shieldin Impacts Radiation and PARPi Sensitivity

Compromised DSB repair is reflected by diminished cell viability after DNA damage. We used clonogenic survival assays to test the relevance of shieldin in cell survival after IR. Consistent with their function in DSB repair, cells depleted of *RINN1–3* were hypersensitive to IR (Figure 6I), showing an important function of shieldin in radiation protection of cells.

53BP1 deletion provides synthetic viability to *BRCA1*-deficient cells; depletion of *53BP1*, as well as of *REV7*, imparts resistance to PARPi in *BRCA1*-defective cells (Bunting et al., 2010; Xu et al., 2015). Based on our finding that shieldin is a key effector of the 53BP1-RIF1 pathway, we posited that depletion of shieldin may modulate PARPi sensitivity. We tested the role of shieldin components in modulating PARPi sensitivity using the specific PARP inhibitor olaparib (Farmer et al., 2005). As expected, *BRCA1*-depleted U2OS cells were highly sensitive to olaparib, but simultaneous depletion of shieldin components rescued cell viability to an extent comparable to that observed with combined depletion of *BRCA1* and *53BP1* (Figure 7A). To confirm these results in a different cell model, we generated a *Rinn1* knockout in $Brca1^{\Delta 11/\Delta 11}$ background (Figure S7F). Consistent with the above results, $Brca1^{\Delta 11/\Delta 11}Rinn^{-/-}$ mouse embryonic fibroblasts (MEFs) showed marked resistance to olaparib (Figure 7B). Collectively, these results show that shieldin functions downstream of 53BP1-RIF1 in imparting PARPi sensitivity in *BRCA1*-deficient cells.

HDR-defective cells show increased frequency of asymmetric radial chromosome structures, which reflect NHEJ-mediated chromosome exchange typical of HDR deficiency. Formation of radial chromosomes in $Brca1^{\Delta 11/\Delta 11}$ cells is dramatically exacerbated by PARPi, and this defect is rescued by deletion of *53bp1* (Bunting et al., 2010). To assess whether RINN1 functions in this pathway, we assessed radial chromosome formation in $Brca1^{\Delta 11/\Delta 11}Rinn^{-/-}$ cells. Indeed, $Brca1^{\Delta 11/\Delta 11}Rinn^{-/-}$ cells showed dramatically reduced frequency of chromosomal aberrations and radial chromosome formation as compared to $Brca1^{\Delta 11/\Delta 11}$ cells (Figure 7C).

Genetic depletion of 53BP1 pathway components can restore HDR in *BRCA1*-deficient cells (Bunting et al., 2010). To test the function of RINN1 in this, we analyzed RAD51 foci in IR-treated $Brca1^{\Delta 11/\Delta 11}$ and $Brca1^{\Delta 11/\Delta 11}Rinn^{-/-}$ cells, as well as in U2OS cells depleted of *BRCA1* alone or in combination with *RINN1*. In the both cell models, depletion of *RINN1* partially restored RAD51 loading in BRCA1-deficient cells (Figure 7D). Furthermore, depletion of *RINN1* recapitulated the established effect of *53BP1* depletion (Bunting et al., 2010) by partially restoring GC-dependent DSB repair in *BRCA1*-depleted cells (Figures 7E and S7G). Together, these results show that deletion of RINN1 can restore HDR, at least partially, in BRCA1-deficient cells, and this may contribute to PARPi resistance in *BRCA1*-deficient cells.

Notably, the chromosomal region encoding *RINN1* and *RINN2* is frequently (~6% each) deleted in the provisional the Cancer Genome Atlas (TCGA) prostate cancer dataset (https://cancergenome.nih.gov), and nearly half of patients with *RINN1* (which was searched with the host gene name *TRAPPC13* because RINN1 is not annotated in this database) and patients with *RINN2* deletion also contain deletion/mutation in genes encoding HDR proteins. This is reminiscent of significantly reduced expression of 53BP1 in *BRCA1*-deficient breast tumors (Bouwman et al., 2010) and implies a potential involvement of shieldin components in cancer that warrants further investigation.

DISCUSSION

This study provides the hitherto most complete, proximity-based quantitative map of the DSB repair networks, demonstrating the potential of the PROX-NET approach in a systematic mapping of neighborhood networks of endogenously expressed, chromatin-associated proteins. A major strength of this approach is that it provides a systems view of spatially resolved neighborhood networks from living cells and has the potential to identify low-affinity, transient, and indirect protein interactions. These strengths of PROX-NET are complementary to the advantages of the traditional AP-MS-based protein-interaction mapping methods, which mostly detect direct protein-protein interactions and thus can provide insights into specific protein complexes and sub-networks within larger interaction networks. We anticipate that the combination of precision nuclease-based APEX tagging of endogenous proteins and PROX-NET will be extendable to map neighborhood networks of other chromatin-associated processes that are “beyond reach” for conventional AP-MS analyses.

Our analyses faithfully captured shared and bait-specific DDR networks, which are highly consistent with previously published literature, and identification of additional DDR factors highlights the usefulness of our dataset in identifying putative novel DDR factors. Notably, our analyses also identified many non-DDR proteins, mostly dominated by proteins related to transcription (for 53BP1) and to centromeres and kinetochores (for BRCA1 and MDC1). In summary, our PROX-NET-based neighborhood networks present a composite picture of DDR and non-DDR-related networks in proximity to 53BP1, BRCA1, and MDC1. The dataset can serve as a resource for further understanding the functions of the bait proteins in DDR and non-DDR related processes.

The function of 53BP1 in DNA damage was reported at the beginning of this millennium (Rappold et al., 2001; Schultz et al., 2000), and cumulative research from the past 17 years established that 53BP1-RIF1-REV7 function in a linear pathway to regulate NHEJ and DSB repair pathway choice. Our work makes several important contributions to the understanding of the 53BP1 pathway: (1) we discover three new proteins that collectively double the number of proteins directly involved in the 53BP1 pathway, (2) we show that these three novel proteins interact with REV7 to form the shieldin complex, (3) we delineate the hierarchy in recruitment of shieldin components to DSB sites, (4) we show that shieldin functions as an 53BP1/RIF1 effector in restraining DNA end resection and promoting NHEJ, and (5) interactions among shieldin components present the first high-affinity direct protein-protein interactions within the 53BP1 pathway.

The prevailing model in DSB repair pathway choice posits that the 53BP1-RIF1 module shields DSBs from DNA end resection. Based on our findings, we expand the current model by including the shieldin complex as an essential downstream module in DSB repair pathway choice (Figure 7F). We propose that 53BP1-RIF1 act upstream to facilitate the recruitment of the shieldin complex, which we postulate shields DSBs against resection and thereby promotes NHEJ. Notably, RINN1–3 are expressed at very low levels, indicating that shieldin is a rate-limiting effector complex in the 53BP1 pathway. Our findings also raise new questions; for example, how is shieldin connected to the upstream components, and what are the structural and biochemical mechanisms by which it inhibits end resection? Identification of RINN1–3 and the shieldin complex presents an important step toward understanding the mechanisms by which cells make key DSB repair decisions.

The work also provides notable insights into the evolution of the 53BP1 pathway and the emergence of antibody class switching. Budding yeast orthologs of 53BP1, RIF1, and REV7 are implicated in the DDR, but their function in DSB repair pathway choice is not evolutionarily conserved in yeast. We show that vertebrate-specific RINN1 acts upstream of REV7; because recently evolved RINN1–3 have key roles in the 53BP1 pathway, we propose that the function of the 53BP1 pathway in DSB repair decision process was added recently. This is consistent with the observation that, unlike the core NHEJ regulators, such as Ku70/Ku80 and LIG4, 53BP1 is not absolutely essential for DNA end joining. However, 53BP1 is critically important for immunoglobulin CSR (Manis et al., 2004), which represents one of the best-known examples of higher vertebrate-specific, NHEJ-dependent physiological process. Immunoglobulin CSR involves generation of activation-induced cytidine deaminase (AID)-induced DSBs in the S regions and subsequent repair by NHEJ. Previously known CSR-regulating factors are present in jawed vertebrates; however, the mammalian-type S regions only evolved in amphibians, and this was thought to have contributed in the evolution of CSR in amphibians. However, B cells from nurse sharks, which do not contain mammalian-type S regions, undergo antigen-induced, AID-dependent CSR (Zhu et al., 2012), demonstrating that a primitive form of CSR evolved prior to the evolution of mammalian-type S regions. Given the contemporary evolution of shieldin (especially of RINN3), as well as its importance for and co-appearance with CSR, it is interesting to speculate that evolution of shieldin may have contributed to the emergence of CSR. In this context, it is notable that nurse sharks, which contain the earliest form of CSR, contain all the members of the shieldin complex.

The 53BP1 pathway is also an important modulator of PARPi sensitivity in HDR-defective tumors. Our results show that deletion of shieldin components provides resistance to PARPi in *BRCA1*-depleted cells. While the clinical relevance of these findings remains to be investigated, our results are entirely consistent with the phenotypes conferred by the previously characterized components of this pathway, including 53BP1, RIF1, and REV7. It would be interesting to investigate the dysregulation and therapeutic relevance of the newly identified shieldin components in cancer.

Collectively, our work provides a panoramic view of the endogenous DDR networks and implicates novel factors in the DDR. The discovery of the shieldin complex provides new insights into the evolution of 53BP1-RIF1-dependent DSB repair pathway choice with

potential implications for understanding higher vertebrate-specific evolution of antibody CSR and clinical resistance to PARP inhibitors.

STAR★METHODS

CONTACT FOR REAGENT AND RESOURCE SHARING

Further information and requests for resources and reagents should be directed to the Lead Contact, Chunaram Choudhary (chuna. choudhary@cpr.ku.dk).

EXPERIMENTAL MODEL AND SUBJECT DETAILS

Cell lines and culture conditions—U2OS, HCT116, HeLa, SH-SY5Y, A549, Kasumi-1, 293FT, hTERT RPE-1, *Brca1*$^{\Delta 11/\Delta 11}$ MEFs and TRF2ts MEFs cells were grown in DMEM medium, and Jurkat cells were grown in RPMI-1640 medium. The source of the cell lines is provided in the Key Resource Table. All cell lines were routinely tested for mycoplasma. The media were supplemented with 10% fetal bovine serum, 1% L-glutamine, 1% penicillin and streptomycin. All cells were cultured in a humidified incubator at 37°C with 5% CO_2 except for TRF2ts MEFs, which were grown at 32°C with 5% CO_2, unless indicated otherwise. For SILAC labeling, cells were grown in media containing either unlabeled amino acids (L-Lysine, L-Arginine), or stable isotope labeled (L-Lysine [4,4,5,5-D4], L-Arginine-U-$^{13}C_6$; L-Lysine-U-$^{13}C_6$, $^{15}N_2$, L-Arginine-U-$^{13}C_6$, $^{15}N_4$) amino acids (Cambridge Isotope Laboratories). Where indicated, cells were irradiated using the YXLON.SMART 160E/1.5 device at the following settings: 160 kV, 6 mA, 14.17 mGy/s. Plasmids were transfected with Lipofectamine 2000 (Invitrogen), while siRNAs were transfected with Lipofectamine RNAiMAX (Invitrogen) as per the manufacturer's instructions.

METHOD DETAILS

Experimental Design—All experiments were performed in replicates. No aspect of the study was done blinded. Sample size was not predetermined and no outliers were excluded.

Plasmids and Cell lines—Human REV7 cDNA from Ultimate ORFeome collection (IOH21465) (Invitrogen) was shuttled into pcDNA-DEST53 vector via Gateway cloning (Thermo Fischer Scientific) to prepare GFP-REV7 fusion construct. Full-length (FL) RINN1 was PCR amplified from U2OS total cDNA and cloned into pcDNA3.1 (+) hygromycin 3x-FLAG vector using KpnI and BamHI restriction sites, generating N-terminal affinity-tagged 3x-FLAG-RINN1. Deletion mutants of RINN1 and RINN1$_{P53A,P58A}$ were prepared in the same vector by sub-cloning and site-directed mutagenesis. siRNA-resistant 3x-FLAG-RINN1 and 3x-FLAG-RINN1$_{P53A,P58A}$ were prepared by site-directed mutagenesis. To prepare GFP-RINN1 construct, RINN1 was PCR amplified and cloned into pEGFP-C1 (Clontech) vector using HindIII and BamHI sites. To prepare Cherry-RINN2 and Cherry-RINN3 expressing plasmids, the respective genes were PCR amplified from U2OS total cDNA and cloned into pmCherry-C1 vector (Clontech) using XhoI/BamHI (RINN2) or XhoI/HindIII (RINN3). Deletion mutants of RINN2 were prepared by sub-cloning and site-directed mutagenesis. To prepare U2OS cell line stably expressing siRNA-resistant 3x-FLAG-RINN1 or 3x-FLAG-RINN$_{1P53A,P58A}$, cells were transfected with the respective

plasmids and selected with hygromycin (200μg/mL). Individual colonies were picked and screened by immunofluorescence and immunoblotting using an antibody against the FLAG epitope. To prepare U2OS cell lines stably expressing GFP-REV7, GFP-RINN1, Cherry-RINN2 and Cherry-RINN3 cells were transfected with the plasmid constructs and selected with G418 (500μg/mL). Individual colonies were picked and screened by GFP or Cherry fluorescence and immunoblotting with REV7, GFP or Cherry antibodies. For knockdown of *Rinn1* and *Rev7* in *Terf2*$^{-/-}$ *Trp53*$^{-/-}$ (TRF2ts) mouse embryonic fibroblasts (MEFs) (Boersma et al., 2015; Konishi and de Lange, 2008), DNA oligos with short hairpins (listed in Table S7) were synthesized and ligated into pSUPER.retro vector (Oligoengine). Retroviral particles were produced by transfecting 293FT cells with pCLeco plasmid, together with pSUPER.retro plasmid. Forty eight hours later, the cell supernatant was harvested and TRF2ts MEFs were transduced. Cells were selected with puromycin (5μg/mL) for 1 week before using them for experiments. To generate shRNA-resistant RINN1 cells in *Rinn1*-depleted TRF2ts background, the sh2 *Rinn1*-transduced MEFs were electroporated with a plasmid encoding GFP-tagged human RINN1 (described above) with Neon transfection system (Invitrogen) according to manufacturer's protocol. The following parameters were used for electroporation; 1,450V, 30mA, and two pulses. The CRISPR/Cas9 technology was utilized to generate CH12 knockout lines of *53bp1*, *Rinn1* and *Rinn3*. Briefly, upon successful cloning of gene-specific gRNAs into PX459 vector, CH12 cells were electroporated with 1μg of the plasmid using electroporation kit L (Lonza, program D-23). 24h following electroporation, cells were selected with puromycin for 48h and the bulk cell population was subjected to single clone isolation. Confirmation of the mutated loci was done through PCR amplification of the targeted region followed by Sanger DNA sequencing.

APEX2-tagging of the endogenous BRCA1, MDC1 and 53BP1—The CRISPR/Cas9 technology was used to fuse three copies of FLAG affinity-tag and APEX2 (3x-FLAG-APEX2) at the N terminus of the endogenous *53BP1*, *BRCA1*, and *MDC1*. U2OS cells were co-transfected with px330 plasmid and a donor plasmid containing puromycin resistance selection gene, P2A self-cleavage site, and 3x-FLAG-APEX2 flanked by homology arms (~500bp each side) corresponding to the respective target genes. The sequences of guide RNAs for targeting *53BP1*, *BRCA1*, and *MDC1* are provided in the Table S7. Puromycin resistant cell clones were screened by genomic PCR using KOD Xtreme hot start DNA polymerase (Millipore) using the primer sequences provided in the Table S7. Positive clones were further validated by monitoring APEX2-dependent protein biotinylation in the engineered cell lines. To knockout *Rinn1* in *Brca1*$^{\Delta 11/\Delta 11}$ MEFs and U2OS, the cells were co-transfected with 4 px330 plasmids expressing *Rinn1* targeting guide RNAs (Table S7) and a donor plasmid containing the puromycin resistance gene. Puromycin-resistant *Brca1*$^{\Delta 11/\Delta 11}$ MEFs were screened by RT-PCR, while U2OS cells were screened by immunoblotting against RINN1 protein.

APEX-based proximity labeling and affinity enrichment of biotinylated proteins—The APEX-expressing cells were incubated with 0.5mM biotin-phenol reagent (Iris Biotech GmbH) for 2 h prior to start of the labeling reaction. The cells were washed with PBS and the labeling reaction was initiated by adding 1mM H_2O_2 in PBS for 2 min at

room temperature. The reaction was terminated by washing cells thrice with a quencher solution containing 10mM sodium azide, 10mM sodium ascorbate, and 5mM Trolox in PBS. Subsequently, the cells were washed twice with ice-cold PBS and cytoplasmic and nuclear fractions were prepared as described previously (Suzuki et al., 2010). The nuclear pellet was lysed with RIPA buffer containing 50mM Tris (pH 7.5), 1M sodium chloride, 1% NP-40, 0.1% sodium deoxycholate, 1mM EDTA, complete protease inhibitor cocktail (Roche), 5mM β-glycerophosphate, 5mM sodium fluoride, and 1mM sodium orthovanadate. Cell lysate was incubated on ice for 10 min before diluting the samples with 4-volumes of RIPA buffer without sodium chloride. Samples were sonicated at amplitude 35 for 1 min. Samples were treated with benzonase for 20 min at room temperature before clarifying the lysate by centrifugation at 12,800 g for 15 min. Clarified lysate was collected and proteins were quantified by Bradford's reagent. Approximately 4mg nuclear lysates from control and bait-expressing cells were mixed 1:1 and incubated with 40μl Strep-Tactin Sepharose beads slurry (IBA Lifesciences) at 4°C on a rotating wheel for overnight. The beads were washed four times with RIPA buffer containing 200mM NaCl and the bound proteins were eluted by boiling the beads at 95°C for 15 min with 50μl 4x NuPAGE LDS sample buffer (Invitrogen) supplemented with 1mM DTT and 5mM biotin.

Sample preparation for MS—Eluates from biotin pull-down were transferred to fresh microfuge tubes and proteins were alkylated with 5.5mM chloroacetamide. The proteins were resolved on a NuPAGE Novex Bis-Tris 4%–12% gel (Invitrogen), the gel was stained with Novex colloidal blue stain (Invitrogen), and subsequently destained with water. Gel lanes for each sample were sliced in to 6 fractions, gel slices were destained further with 25mM ammonium bicarbonate buffer containing 50% ethanol. Gel pieces were dehydrated with 100% ethanol and proteins were in-gel digested with trypsin (Sigma) at 37°C for 16h. Trypsin digestion was stopped by incubating the gel pieces with trifluoroacetic acid and the resulting peptides were eluted with increasing concentration of acetonitrile and desalted on reversed-phase C18 StageTips. The peptides were eluted from StageTips by adding 40μl of elution buffer containing 60% acetonitrile and 0.1% trifluoroacetic acid. Acetonitrile concentration in the eluates was reduced to less than 5% by vacuum centrifugation and peptides were diluted with a buffer containing 0.5% acetic acid and 0.1% trifluoroacetic acid before injecting into a mass spectrometer.

GFP pull-downs and MS sample preparation—U2OS cells expressing either GFP, GFP-RINN1, or GFP-REV7 were either left untreated or were irradiated with ionizing radiation (4Gy), and after 1 h recovery cells were lysed with RIPA buffer containing 50mM Tris (pH 7.5), 150mM sodium chloride, 0.5% NP-40, 0.1% sodium deoxycholate, 5% Glycerol, 1mM EDTA, complete protease inhibitor cocktail (Roche), 5mM β-glycerophosphate, 5mM sodium fluoride, 1mM sodium orthovanadate, and benzonase (250U/ml). Cell lysates were incubated on ice for 30 min and lysates were clarified by centrifuging at 12,800 g for 15 min at 4°C. Protein concentration was quantified using Quick Start Bradford Protein Assay (Bio-Rad) and ~5mg clarified lysates were incubated with 15μl GFP-Trap magnetic beads (ChromoTek GmbH) for 2 h on a rotating wheel at 4°C. The beads were subsequently washed thrice with ice-cold RIPA lysis buffer, and subsequently the bound proteins were eluted by boiling the beads at 95°C for 15 min with 50μl 4x

NuPAGE LDS sample buffer (Invitrogen) supplemented with 1mM DTT. The eluted proteins were in-gel digested and prepared for MS analysis as described above.

MS analyses—Peptides were analyzed on a quadrupole Orbitrap mass spectrometer (Q-Exactive plus HF, Thermo Scientific) equipped with a nanoflow HPLC system (Thermo Scientific). Peptides were loaded onto C18 reversed-phase columns (15 cm length, 75 μm inner diameter) and eluted with a linear gradient of 8 to 40% acetonitrile containing 0.5% acetic acid. The mass spectrometer was operated in a data-dependent mode, automatically switching between MS and MS/MS acquisition. Survey full-scan MS spectra (m/z 300 – 1750) were acquired in the Orbitrap. The 10 most intense ions were sequentially isolated and fragmented by higher-energy C-trap dissociation (HCD). An ion selection threshold of 50,000 counts was used. Peptides with unassigned charge states, as well as with charge state less than +2 were excluded from fragmentation. Fragment spectra were acquired in the Orbitrap mass analyzer.

Annotation of biological pathways and Gene Ontology analysis—The proteins that are involved in the DNA damage response, DNA replication, or telomere maintenance pathways were retrieved using ConsensusPathDB v32 (http://cpdb.molgen.mpg.de), AmiGO (http://amigo.geneontology.org/amigo), and from manually curated references. Proteins were grouped in to sub-pathways and protein complexes based on references and expert knowledge. Many of the enriched proteins have been implicated in different pathways and form different protein complexes, in the networks each protein is assigned to one pathway or protein complex to avoid redundancy. The Gene Ontology term enrichment analysis was performed using AmiGO 2 online tool (http://amigo.geneontology.org/amigo).

Construction of de-novo networks—The SILAC ratios of significant PROX-NET interactors from 18 experiments (six replicates, three baits) were used for constructing the de-novo networks. If the SILAC ratio of an interactor was greater than the SILAC ratio of the bait, it was replaced by the bait value, and missing or the negative values were replaced with 0. In the PROX-NET dataset, many interactors were only detected or quantified in specific experiments and the SILAC ratios were missing in the remaining experiments. To calculate a similarity scores for proteins with missing SILAC ratio, we used random sampling to estimate the dissimilarity score distribution of the null models for each protein. Ten thousand random datasets were generated by sampling the values from each experiment, the differential score $S_{XY,b,r}$ for two proteins X and Y having corresponding values $X_{b,r}$ and $Y_{b,r}$ in each experiment is defined as

$$S_{XY,b,r} = |X_{b,r} - X_{b,r}|$$

where b is the bait and r is the biological replicates. The dissimilarity score between protein X and Y was calculated as a root of the squared sum of the differential score, $S_{XY,b,r}$

$$dissimilarity\ score = \sqrt{\sum_{b}\sum_{r} S_{XY,b,r}{}^{2}}$$

The dissimilarity score distribution of a protein against the random dataset was estimated in a protein-wise manner, and the p value was determined based on the null model distribution. This yielded two p values per protein pair, we took the higher (i.e., more conservative) p value and Benjamini Hochberg method was applied for multiple correction comparison. Protein-protein interaction pairs with the adjusted p value < 0.01 were regarded to be significant. To group the proteins in the de-novo networks, the Markov Clustering (MCL) was used with the parameter of inflation 1.2, resulting in six network clusters. Statistical analyses and data visualization was performed using the R environment. The interaction networks were visualized with Cytoscape 3.5 (http://www.cytoscape.org).

Immunoprecipitation and immunoblotting—To analyze the interaction between RINN1 and REV7, a plasmid with 3x-FLAG-RINN1 was transiently transfected in 293FT cells using Lipofectamine 2000 (Invitrogen). Twenty four hours later, cells were either left untreated or were irradiated with ionizing radiation (4Gy). Following 1h recovery, cells were harvested and lysed in ice-cold RIPA buffer containing 50mM Tris (pH 7.5), 150mM sodium chloride, 0.5% NP-40, 0.1% sodium deoxycholate, 5% Glycerol, 1mM EDTA, complete protease inhibitor cocktail (Roche), 5mM β-glycerophosphate, 5mM sodium fluoride, 1mM sodium orthovanadate, and benzonase (250U/ml). Cell lysates were incubated on ice for 30 min and clarified by centrifuging at 12,800 g for 15 min at 4°C. Protein concentration was quantified using Quick Start Bradford Protein Assay (Bio-Rad) and ~5mg clarified lysates were incubated with 15μl anti-FLAG M2 magnetic beads (Sigma) for 2h on a rotating wheel at 4°C. The beads were subsequently washed once with RIPA lysis buffer and twice with ice-cold TBS buffer (50mM Tris-HCl, pH 7.4, with 150mM NaCl). Subsequently, the bound proteins were eluted by incubating the beads with 3x-FLAG peptide (300ng/μl, Sigma) in TBS buffer for 30 min at 4°C with gentle shaking. The eluates were mixed with 4x NuPAGE LDS sample buffer (Invitrogen) supplemented with 1mM DTT and samples were boiled at 95°C for 15 min before resolving them on SDS-PAGE (NuPAGE Novex Bis-Tris 4%–12% gels, Invitrogen). Proteins were transferred onto nitrocellulose membranes, and the membranes were blocked with 5% skimmed milk powder (Sigma) solution in PBS with 0.1% Tween-20 (Sigma) for 1h at room temperature. The membranes were incubated with antibodies diluted in 5% BSA for overnight at 4°C. Horseradish peroxidase-conjugated secondary α-mouse, α-sheep, or α-rabbit antibodies (Jackson ImmunoResearch Laboratories) and Novex ECL chemiluminescence (Invitrogen) were used for immunodetection. Interaction between ectopically expressed 3x-FLAG-RINN1 mutants with endogenously expressed REV7 was analyzed in 293FT cells by co-immunoprecipitation as described above.

To analyze the interaction between REV7 and RINN1, U2OS cells stably expressing GFP-REV7 were either left untreated or were irradiated with ionizing radiation (4Gy), and after 1 h recovery cell lysates were prepared as described in the above section. About 5mg of clarified lysates were incubated with 15μl GFP-Trap magnetic beads (ChromoTek GmbH) for 2 h on a rotating wheel at 4°C. The beads were subsequently washed thrice with ice-cold RIPA lysis buffer, the bound proteins were eluted and resolved on SDS-PAGE (NuPAGE Novex Bis-Tris 4%–12% gels, Invitrogen), and immunoblotted as described above.

To probe interaction of RINN2 and RINN3 with RINN1 and REV7, U2OS cells stably expressing Cherry-RINN3 and Cherry-RINN2 were either left untreated or were irradiated with ionizing radiation (4Gy), and after 1 h recovery cell lysates were prepared as described above. About 2mg of clarified lysates were incubated with 15μl GFP-Trap magnetic beads (ChromoTek GmbH) for 2 h on a rotating wheel at 4°C. The beads were subsequently washed thrice with ice-cold RIPA lysis buffer, the bound proteins were eluted and resolved on SDS-PAGE (NuPAGE Novex Bis-Tris 4%–12% gels, Invitrogen), and immunoblotted as described above. Interactions were analyzed using co-immunoprecipitation and immunoblotting as described above.

For the experiments related to mapping of interaction-domains in RINN1 and RINN2, 293FT cells were transiently transfected with the indicated constructs and immunoprecipitation was performed as described above using anti-FLAG (for FLAG-RINN1 constructs) or anti-RFP (for Cherry-RINN2 constructs) affinity matrix.

Generation of RINN1 antibody—A sheep polyclonal antibody against RINN1 was raised (at the antibody production facility at University of Dundee) by immunization with a full-length, bacterially-produced recombinant GST-fusion protein. The specificity of this antibody was validated by depleting *RINN1* with siRNA.

Cell Synchronization—U2OS cells were treated with 2mM thymidine for 18h and released in fresh medium for 16h. Thymidine (2mM) was added again, and cells were incubated for another 12h in order to arrest cells in G1 phase before releasing them again in fresh medium. Cells were collected at the indicated time points, lysed in RIPA buffer, proteins were separated on SDS-PAGE, and immunoblotted against endogenously expressed RINN1, REV7, Cyclin A, Cyclin E and phospho-Histone 3 (Ser10).

Expression analysis of RINN1 and REV7 in cell lines—U2OS, HCT116, HeLa, SH-SY5Y, A549, Kasumi-1, 293FT, hTERT RPE-1 and Jurkat cells were collected and lysed in RIPA buffer. Cell lysates were cleared by centrifugation and proteins were quantified with Quick Start Bradford Protein Assay Kit (Bio-Rad). Equal amount of protein was loaded on SDS-PAGE and expression of RINN1 and REV7 was probed by immunoblotting with RINN1 and REV7 antibodies.

Metaphase chromosome analyses—To prepare metaphase spreads for chromosome analyses, shRNA-transduced TRF2ts MEFs were either cultured at 32°C or 39°C for 24h before incubating them with KryoMAX colcemid solution (0.1μg/ml) (Thermo Fisher Scientific) for 2h. Cells were collected and incubated with 75mM KCl solution at 37°C for 20 min. Cells were spun down at 400 g for 7 min and fixed with methanol-acetic acid solution (3:1 v/v) for 20 min at room temperature. Metaphases were obtained by dropping the cell suspensions on ice-cold humidified glass slides. For telomere FISH analyses, glass slides with metaphase spreads were aged at 65°C for 10 min. Slides were immersed in PBS for 15 min before fixing them with 4% formaldehyde in PBS for 4 min. Slides were washed with PBS twice and immersed in 0.005% pepsin solution in 0.01M HCl at 37°C for 8 min. Slides were washed twice with PBS and dehydrated for 2 min each in cold ethanol series (70%, 90% and 100%). Air-dried slides were covered with TelC-Cy3 probe (50μg/ml)

(Panagene, F1002) in hybridization buffer (10mM Na_2HPO_4, 10mM NaCl, 20mM Tris (pH 7.5), 70% formamide) and incubated for 5 min at 80°C. Slides were further incubated for 2h at 37°C in dark and were washed thrice with washing buffer I (0.1% tween 20 in PBS) and one time with washing buffer II (0.1% tween 20 in 300mM NaCl and 30mM tri-Sodium citrate dihydrate) at room temperature. Slides were further washed for 2 min each in cold ethanol series as described above and air-dried before mounting them with VECTASHIELD containing DAPI (Vector Laboratories, H-1200). For statistical analyses, at least 50 metaphases per experiment were imaged using Zeiss Axio Imager.A2 equipped with EC Plan-NEOFLUAR 63x oil objective, and an AxioCam MRm camera. Images were acquired and processed uniformly using ZEN pro2011 software (Zeiss).

To quantify chromosomal aberrations in *Brca1*$^{\Delta 11/\Delta 11}$ and *Brca1*$^{\Delta 11/\Delta 11}$*Rinn*$^{-/-}$ cells, the cells were treated with 1 μM PARPi (olaparib) for 22 hours before preparing metaphase spreads as described above. In each experiment, 40 metaphases were scored for the presence of chromosomal aberrations (i.e., radials, chromosome breaks, chromatid breaks and chromosome fusions).

Sample preparation for immunofluorescence and QIBC—Cells for microscopy-based experiments were cultured on 12mm-round, 1.5mm-thick cleaned glass coverslips in 12-well plates. Cells were either left untreated or irradiated as described above. Cells were pre-extracted with ice-cold PBS containing 0.2% Triton X-100 (Sigma-Aldrich) for 2 min on ice before fixing them with 4% buffered formaldehyde solution at room temperature for 10 min. To perform Click-iT EdU staining, cells were incubated with 10μM EdU for 30 min before pre-extraction and fixation, and EdU labeling was detected as recommended by the manufacturer (Thermo Fisher Scientific). Cells were incubated with primary-antibodies in a filtered DMEM medium supplemented with 10% fetal bovine serum and 0.05% sodium azide for 2h at room temperature. Coverslips were washed thrice with PBS containing 0.2% Tween 20 (Sigma-Aldrich) and fluorophore-conjugated secondary-antibodies supplemented with 0.5μg/ml 4′,6-diamidino-2-phenylindole dihydrochloride (DAPI) were applied for 30 min at room temperature. Coverslips were subsequently washed thrice with PBS-Tween 20, twice in distilled water, air-dried and mounted in 5μl Mowiol-based mounting medium (Mowiol 488, Calbiochem in glycerol/Tris-HCl pH8.5 buffer). To detect DSB induced DNA end-resection, the cells were labeled for 10 μM BrdU for 30 h, and then released into fresh growth medium prior to irradiation. Samples were processed as indicated for IF protocol under native conditions using mouse anti-BrdU antibody (BD PharMingen) for 60 min at room temperature followed by Alexa 488 goat anti-mouse (Invitrogen) secondary antibody.

QIBC was performed as previously described (Toledo et al., 2013) with the following modifications and adjustments. Images were acquired with a ScanR inverted microscope High-content Screening Station (Olympus) equipped with wide-field optics, a 20x, 0.75-NA (UPLSAPO 20x) dry objective, fast excitation and emission filter-wheel devices for DAPI, FITC, Cy3, and Cy5 wavelengths, an MT20 illumination system, and a digital monochrome Hamamatsu ORCA-R2 CCD camera (yielding a spatial resolution of 320 nm per pixel at 20x and binning of 1). Images were acquired in an automated fashion with the ScanR acquisition software (Olympus, 2.6.1). Depending on cell confluency, 49 to 81 images were acquired containing at least 500 cells per condition. Acquisition times for the different

channels were adjusted for nonsaturated conditions in 12-bit dynamic range, and identical settings were applied to all the samples within one experiment.

Confocal microscopy—Confocal images were acquired with an UltraVIEW Vox spinning-disk microscope (Perkin Elmer) and Volocity software (Version 6.3). The microscope is equipped with a 60x, 1.4NA Plan-Apochromat oil-immersion objective lens and with appropriate filter sets for excitation and emission up to four different wavelengths. Images were recorded with a Hamamatsu EMCCD 16-bit camera at a spatial resolution of 121 nm (x, y) and 250 nm in the z dimension. Within a series of experiments, laser power and exposure time were appropriately adjusted with identical settings to avoid saturating intensities.

Clonogenic survival assay—For colony survival assay, U2OS cells were transfected with 20nM of the indicated siRNAs for 48h, seeded onto 6-well plates (1000 cells per well), and treated with the indicated concentration of olaparib or with IR as specified in the figure legends. After 9 days, cells were fixed with buffered 4% formaldehyde solution and stained with 0.1% crystal violet. Individual colonies were counted manually and the percentage survival was calculated as values for indicated siRNAs divided by values for control siRNA, after correcting for the respective plating efficiency. The same approach was used to determine clonogenic potential of $Brca1^{\Delta 11/\Delta 11}$ and $Brca1^{\Delta 11/\Delta 11}Rinn^{-/-}$ cells treated with different concentration of olaparib.

DR-GFP and EJ5-GFP reporter assays—To quantify the repair of I-SceI-generated DBSs by gene conversion, U2OS DR-GFP cells were transfected with the indicated siRNAs, and 24h later cells were transfected with either an empty vector as control or with 25μg of the I-SceI expression vector pCBASce using Lipofectamine LTX (Thermo Fisher Scientific). The GC efficiency was determined 72hr later, by quantifying GFP-positive cells by flow cytometry with a FACS SH800 (Sony Biotechnology). XRCC3 was included as a positive control in these assays.

To measure the repair of I-SceI-generated DSBs by NHEJ, U2OS EJ5-GFP cells were transfected with the indicated siRNAs, and 24h later cells were transfected with 25μg of the I-SceI expression vector pCBASce or an empty vector using Lipofectamine LTX (Thermo Fisher Scientific). The NHEJ efficiency was determined 72hr later, and GFP-positive cells were quantified by flow cytometry as described above.

CSR assay in CH12 cells—CH12 cells were cultured and stimulated with 250ng/mL CD40L, 10ng/mL IL4 and 1ng/mL TGFβ (CIT) to induce class switching to IgA. For siRNA-based knockdown experiments, transfection of siRNA oligonucleotide (Invitrogen) into CH12 cells was done using electroporation kit (Lonza). The cells were subsequently cultured for 24 hours before the addition of CIT and incubated further for an additional 24 hours. For FACS analysis, the cells were labeled with FITC-conjugated anti-IgM (ThermoFisher Scientific) and PE-conjugated anti-IgA (Southern Biotech). All analyses were performed on FACS Calibur (Becton Dickinson).

RT-PCR analysis in CH12 cells—Total RNA derived from CH12 cells were extracted and isolated using TRIzol (Ambion). The cDNA was synthesized using SuperScript SuperMix (Invitrogen) followed by real-time PCR using specific primers and SYBR Green Supermix (Biorad).

Expression and purification of recombinant proteins—Previous studies showed that despite the small size, production of recombinant REV7 is not amenable to standard bacterial expression protocol. Mutation of R124 in REV7 ($REV7_{R124A}$) can stabilize the protein, allowing purification of recombinant $REV7_{R124A}$ (Hara et al., 2009). Full length REV7 was expressed as His_6-tagged protein from a pET-Duet-1 vector (Novagen). $RINN1_{28–83}$ was expressed as GST-fusion protein using the modified pGEX-4T5/Tev vector, which is derived from pGEX-4T1 (GE healthcare). The GST-tag was removed with TEV-protease for $RINN1_{28–83}$. The REV7·$RINN1_{f.l.}$, and REV7·$RINN1_{28–83}$ complexes were expressed in *E. coli* BL21 (DE3) cells using pRSF-Duet-1, and a modified pRSF-Due1 containing a TEV-cleavage site to remove the N-terminal His_6-tag. All proteins were of human origin. Cells were grown in TB-medium up to an OD_{600} of 0.6 (37°C; 160 rpm). Protein expression was induced by adding 300 μM of isopropyl-β-D-thiogalactopyranoside (IPTG) and was done overnight at 160 rpm, 18°C. The cells were harvested by centrifugation (4,500 rpm, 10 min) and resuspended in buffer A (50 mM Tris/HCl pH7.4, 100 mM NaCl, 5 mM $MgCl_2$, 2 mM β–mercaptoethanol) plus 100 μM Pefabloc as protease inhibitor. After cell lysis by sonication, the protein containing soluble cell fraction was obtained after centrifugation (20,000 rpm, 45 min). This fraction was applied to the equilibrated affinity-chromatography column. Unbound and unspecifically bound proteins were washed off using high-salt buffer B (50 mM Tris/HCl pH 7.4, 300 mM NaCl, 5 mM $MgCl_2$, 2 mM β-mercaptoethanol; Ni-NTA: plus 20 mM imidazole). To remove the GST-tag, TEV-protease cleavage was done on the column over night at 4°C in buffer A. For the His_6-tag, the eluted protein was desalted using a HiPrep 26/10 Desalting column (GE healthcare) to remove the imidazole before addition of TEV-protease. After TEV-cleavage the eluate was concentrated by ultrafiltration and purification was continued performing a size-exclusion chromatography (GE healthcare) in buffer C (50 mM Tris/HCl pH 7.4, 100 mM NaCl, 5 mM $MgCl_2$, 2 mM β-mercaptoethanol). The fractions containing the protein were flash frozen in liquid nitrogen and stored at −80°C. Protein concentrations were determined using the absorption at 280 nm with the extinction coefficient calculated for the protein.

Analytical size-exclusion chromatography—Analytical size-exclusion chromatography runs were performed on a Superdex S75 10/300 GL column (GE healthcare) using buffer A (50 mM Tris/HCl pH7.4, 100 mM NaCl, 5 mM $MgCl_2$, 2 mM β–mercaptoethanol). 600 μg of His_6-REV7 and 126 μg of $RINN1_{28–83}$ were used for the runs alone. 600 μg His_6-REV7 was mixed with 126 μg of $RINN1_{28–83}$ (1.2-fold molar excess of REV7 to RINN1) and incubated for 30 min on ice to preform the complex prior to the SEC run. The His_6-REV7, $RINN1_{28–83}$ alone and the His_6-REV7·$RINN1_{28–83}$ complex was loaded on the calibrated column using a 100 μl injection loop. The fractions obtained from the SEC runs with His_6-REV7, $RINN1_{28–83}$ alone and from run with the preformed His_6-REV7·$RINN1_{28–83}$ complex were analyzed by 20% SDS-PAGE.

Isothermal titration calorimetry (ITC) measurements—The interaction of Rev7 and $RINN1_{28–83}$ was thermodynamically characterized using isothermal titration calorimetry (ITC) on an ITC_{200} instrument (Malvern Instruments). All measurements were done in ITC buffer containing 50 mM Tris/HCl pH7.4, 100 mM NaCl, 5 mM $MgCl_2$, 2 mM β–mercaptoethanol. 2 μl of $RINN1_{28–83}$ in the syringe (300 μM or 500 μM) was stepwise injected into the cell containing full-length REV7 (20, 30 or 300 μM). The heating power per injection was recorded and plotted as a function of time until binding saturation was achieved. The binding isotherms were fitted to a one-site-binding model using the MicroCal software. Thereby, the the stoichiometry of binding (N), the enthalpy change (ΔH) and the equilibrium-association constant (K_A) were obtained as primary data. ΔS (TΔS) and the equilibrium-dissociation constant (K_D) are derived. We used the standard EDTA-$CaCl_2$ sample tests to assess the statistical significance of individual observations as described by MicroCal. The values determined were within the tolerances of ± 20% for K_A values and ± 10% in ΔH as suggested by the manufacturer.

QUANTIFICATION AND STATISTICAL ANALYSIS

Peptide identification and MS data analyses—The raw MS data files were analyzed using MaxQuant. A UniProt database against human proteome obtained from the UniProtKB (downloaded July 06, 2015) was used to search for parent ion and MS/MS spectra using the integrated Andromeda search engine (Cox et al., 2011). Tandem mass spectra were searched with a mass tolerance of 6 ppm in MS mode, 20 ppm in HCD MS2 mode, strict trypsin specificity and allowing max. 2 missed cleavage sites. N-terminal protein acetylation, and methionine oxidation were searched as variable modifications, whereas cysteine carbamidomethylation was searched as a fixed modification. The dataset was filtered based on posterior error probability (PEP) to arrive at a false discovery rate of below 0.01 estimated using a target-decoy approach.

The ProteinGroups output table from MaxQuant was filtered to remove “Potential contaminant,” “Reverse” decoy database entries, and entries with “Only identified by site.” Furthermore, proteins with less than 2 peptides, and proteins without unique peptides were removed. For the protein groups where multiple genes are assigned, the first gene name or, if not available, the first UniProt ID is used as a representative protein name. After filtering the tables, the SILAC ratio of “heavy” to “light” (H/L) is transformed to $\log_2$ ratio and normalized with a mean of 0 and a standard deviation of 1 (hereafter normalized ratios). In the PROX-NET dataset, the proteins that fulfill all the following criteria are regarded as significantly enriched: (1) the minimum number of the unique peptides is ≥ 2, (2) protein is quantified in at least two replicate experiments (out of six) for a given bait, (3) the mean of the normalized $\log_2$ SILAC ratio is ≥ 0.95. For identifying significantly enriched interactors of endogenously expressed 3x-FLAG-APEX2–53BP1, -BRCA1, and -MDC1, from the FLAG affinity-purification mass spectrometry (AP-MS) analyses, the proteins with mean SILAC $\log_2$ ratio (bait/control) ≥ 1, and the SILAC $\log_2$ ratio (bait/control) ≥ 1 in at least two experiments were regarded as significant interactors.

For identifying significantly enriched interactors of ectopically expressed GFP-RINN1 and GFP-REV7 from the label-free IP datasets, the bait/control iBAQ ratios were calculated.

Missing iBAQ values in the control dataset were imputed with 1,000. The iBAQ ratios of bait/control were $\log_2$-transformed and normalized with a mean of 0 and a standard deviation of 1, mean iBAQ ratios from four replicates were used to identify the significantly enriched proteins. The proteins with $\log_2$ iBAQ ratios (bait/control) ≥ 0.95, and captured in at least two out of four replicates were defined as significant interactors.

QIBC analyses—For QIBC analyses, images were processed and analyzed with ScanR analysis software. First, a dynamic background correction was applied to all images. The DAPI signal was then used for the generation of an intensity-threshold-based mask to identify individual nuclei as main objects. This mask was then applied to analyze pixel intensities in different channels for each individual nucleus. After segmentation of nucleus, the desired parameters for the different nuclei or foci were quantified, with single parameters (mean and total intensities, area, foci count, and foci intensities) as well as calculated parameters (sum of foci intensity per nucleus). These values were then exported and analyzed with TIBCO Software, version 5.0.0. This software was used to quantify absolute, median, and average values in cell populations and to generate color-coded scatterplots. Within one experiment, similar cell numbers were compared for the different conditions, and for visualization low x axis jittering was applied (random displacement of objects along the x axis) to make overlapping markers visible.

Statistical analyses—For QIBC data, statistical significance was calculated using approximative Wilcoxon-Mann-Whitney Test. At least 500 cells were analyzed per replicate, n = 2–3.

For calculating statistical significance for NHEJ efficiency, gene conversion efficiency, IgA class switch recombination assay, cell survival assays and chromosome abnormalities in $Brca1^{\Delta 11/\Delta 11}$ and $Brca1^{\Delta 11/\Delta 11}Rinn1^{-/-}$ cells after treatment with olaparib, a Student's t-Test was used, n = 3–6.

For chromosome fusion assay, statistical significance was calculated using a Cochran–Mantel–Haenszel test. At least 2000 chromosomes were analyzed per replicate, n = 2. For all statistical analyses, Benjamini-Hochberg correction is used for multiple hypothesis testing. Results were considered significant if the P value was < 0.05.

DATA AND SOFTWARE AVAILABILITY

The mass spectrometry raw data reported in this paper have been deposited to the ProteomeXchange Consortium via the PRIDE partner repository with the dataset identifier PRIDE: PXD009284.

Supplementary Material

Refer to Web version on PubMed Central for supplementary material.

ACKNOWLEDGMENTS

We thank the members of our laboratories for their help and useful discussions. We thank Rebeca Soria Romero for her excellent technical assistance. R.G. is supported by the EMBO long-term postdoctoral fellowship

(ALTF271-2014). A.S. is supported by Human Frontier Science Foundation long-term fellowship (LT000129/2015). C.C. is supported by the Hallas Møller Investigator Fellowship from the Novo Nordisk Foundation (NNF14OC0008541). This project has received funding from the European Research Council (ERC) under the European Union's Horizon 2020 research and innovation program (grant agreement 648039). M.L. is supported by Heisenberg Fellowship of the German Research Foundation (Deutsche Forschungsgemeinschaft [DFG; LA 2984/3-1]). M.K. is funded by the Cologne Graduate School of Ageing Research (CGA). The A.N. laboratory is supported by the Intramural Research Program of the NIH, an Ellison Medical Foundation Senior Scholar in Aging Award, the Department of Defense Idea Expansion and Breakthrough Awards, and the Alex Lemonade Stand Foundation Award. We thank Jacqueline Jacobs and Titia de Lange for providing the TRF2ts MEF cell line and Özgun Özer from the Ian D. Hickson laboratory for her helpful discussions on the telomere FISH analysis. We thank the CPR Mass Spectrometry Platform and the CPR Protein Imaging Platform for their technical assistance. The Center for Chromosome Stability is supported by the Danish National Research Foundation (DNRF 115). The Novo Nordisk Foundation Center for Protein Research is supported financially by the Novo Nordisk Foundation (NNF14CC0001).

REFERENCES

Bekker-Jensen S, Lukas C, Melander F, Bartek J, and Lukas J (2005). Dynamic assembly and sustained retention of 53BP1 at the sites of DNA damage are controlled by Mdc1/NFBD1. J. Cell Biol 170, 201–211. [PubMed: 16009723]

Bodenhofer U, Bonatesta E, Horejš-Kainrath C, and Hochreiter S (2015). msa: an R package for multiple sequence alignment. Bioinformatics 31, 3997–3999. [PubMed: 26315911]

Boersma V, Moatti N, Segura-Bayona S, Peuscher MH, van der Torre J, Wevers BA, Orthwein A, Durocher D, and Jacobs JJL (2015). MAD2L2 controls DNA repair at telomeres and DNA breaks by inhibiting 5′ end resection. Nature 521, 537–540. [PubMed: 25799990]

Bouwman P, Aly A, Escandell JM, Pieterse M, Bartkova J, van der Gulden H, Hiddingh S, Thanasoula M, Kulkarni A, Yang Q, et al. (2010). 53BP1 loss rescues BRCA1 deficiency and is associated with triple-negative and BRCA-mutated breast cancers. Nat. Struct. Mol. Biol 17, 688–695. [PubMed: 20453858]

Bryant HE, Schultz N, Thomas HD, Parker KM, Flower D, Lopez E, Kyle S, Meuth M, Curtin NJ, and Helleday T (2005). Specific killing of BRCA2-deficient tumours with inhibitors of poly(ADP-ribose) polymerase. Nature 434, 913–917. [PubMed: 15829966]

Bunting SF, Callén E, Wong N, Chen HT, Polato F, Gunn A, Bothmer A, Feldhahn N, Fernandez-Capetillo O, Cao L, et al. (2010). 53BP1 inhibits homologous recombination in Brca1-deficient cells by blocking resection of DNA breaks. Cell 141, 243–254. [PubMed: 20362325]

Ceccaldi R, Rondinelli B, and D'Andrea AD (2016). Repair Pathway Choices and Consequences at the Double-Strand Break. Trends Cell Biol 26, 52–64. [PubMed: 26437586]

Chapman JR, Barral P, Vannier JB, Borel V, Steger M, Tomas-Loba A, Sartori AA, Adams IR, Batista FD, and Boulton SJ (2013). RIF1 is essential for 53BP1-dependent nonhomologous end joining and suppression of DNA double-strand break resection. Mol. Cell 49, 858–871. [PubMed: 23333305]

Chatr-Aryamontri A, Oughtred R, Boucher L, Rust J, Chang C, Kolas NK, O'Donnell L, Oster S, Theesfeld C, Sellam A, et al. (2017). The BioGRID interaction database: 2017 update. Nucleic Acids Res 45 (D1), D369–D379. [PubMed: 27980099]

Chaudhuri J, Basu U, Zarrin A, Yan C, Franco S, Perlot T, Vuong B, Wang J, Phan RT, Datta A, et al. (2007). Evolution of the immunoglobulin heavy chain class switch recombination mechanism. Adv. Immunol 94, 157–214. [PubMed: 17560275]

Chen LY, Redon S, and Lingner J (2012). The human CST complex is a terminator of telomerase activity. Nature 488, 540–544. [PubMed: 22763445]

Cong L, Ran FA, Cox D, Lin S, Barretto R, Habib N, Hsu PD, Wu X, Jiang W, Marraffini LA, and Zhang F (2013). Multiplex genome engineering using CRISPR/Cas systems. Science 339, 819–823. [PubMed: 23287718]

Conomos D, Reddel RR, and Pickett HA (2014). NuRD-ZNF827 recruitment to telomeres creates a molecular scaffold for homologous recombination. Nat. Struct. Mol. Biol 21, 760–770. [PubMed: 25150861]

Cox J, Neuhauser N, Michalski A, Scheltema RA, Olsen JV, and Mann M (2011). Andromeda: a peptide search engine integrated into the MaxQuant environment. J. Proteome Res 10, 1794–1805. [PubMed: 21254760]

Crabbe L, Verdun RE, Haggblom CI, and Karlseder J (2004). Defective telomere lagging strand synthesis in cells lacking WRN helicase activity. Science 306, 1951–1953. [PubMed: 15591207]

Di Paolo A, Racca C, Calsou P, and Larminat F (2014). Loss of BRCA1 impairs centromeric cohesion and triggers chromosomal instability. FASEB J 28, 5250–5261. [PubMed: 25205741]

Difilippantonio S, Gapud E, Wong N, Huang CY, Mahowald G, Chen HT, Kruhlak MJ, Callen E, Livak F, Nussenzweig MC, et al. (2008). 53BP1 facilitates long-range DNA end-joining during V(D)J recombination. Nature 456, 529–533. [PubMed: 18931658]

Escribano-Díaz C, Orthwein A, Fradet-Turcotte A, Xing M, Young JT, Tkáč J, Cook MA, Rosebrock AP, Munro M, Canny MD, et al. (2013). A cell cycle-dependent regulatory circuit composed of 53BP1-RIF1 and BRCA1-CtIP controls DNA repair pathway choice. Mol. Cell 49, 872–883. [PubMed: 23333306]

Farmer H, McCabe N, Lord CJ, Tutt AN, Johnson DA, Richardson TB, Santarosa M, Dillon KJ, Hickson I, Knights C, et al. (2005). Targeting the DNA repair defect in BRCA mutant cells as a therapeutic strategy. Nature 434, 917–921. [PubMed: 15829967]

Flynn RL, Centore RC, O'Sullivan RJ, Rai R, Tse A, Songyang Z, Chang S, Karlseder J, and Zou L (2011). TERRA and hnRNPA1 orchestrate an RPA-to-POT1 switch on telomeric single-stranded DNA. Nature 471, 532–536. [PubMed: 21399625]

Gaillard H, and Aguilera A (2016). Transcription as a Threat to Genome Integrity. Annu. Rev. Biochem 85, 291–317. [PubMed: 27023844]

GTEx Consortium (2013). The Genotype-Tissue Expression (GTEx) project. Nat. Genet 45, 580–585. [PubMed: 23715323]

Hara K, Shimizu T, Unzai S, Akashi S, Sato M, and Hashimoto H (2009). Purification, crystallization and initial X-ray diffraction study of human REV7 in complex with a REV3 fragment. Acta Crystallogr. Sect. F Struct. Biol. Cryst. Commun 65, 1302–1305.

Hothorn T, Hornik K, van de Wiel MA, and Zeileis A (2008). Implementing a Class of Permutation Tests: The coin Package. J. Stat. Soft 28.

Hustedt N, and Durocher D (2016). The control of DNA repair by the cell cycle. Nat. Cell Biol 19, 1–9. [PubMed: 28008184]

Jackson SP, and Bartek J (2009). The DNA-damage response in human biology and disease. Nature 461, 1071–1078. [PubMed: 19847258]

Kappei D, Butter F, Benda C, Scheibe M, Draškovič I, Stevense M, Novo CL, Basquin C, Araki M, Araki K, et al. (2013). HOT1 is a mammalian direct telomere repeat-binding protein contributing to telomerase recruitment. EMBO J 32, 1681–1701. [PubMed: 23685356]

Konishi A, and de Lange T (2008). Cell cycle control of telomere protection and NHEJ revealed by a ts mutation in the DNA-binding domain of TRF2. Genes Dev 22, 1221–1230. [PubMed: 18451109]

Kumar S, Stecher G, Suleski M, and Hedges SB (2017). TimeTree: A Resource for Timelines, Timetrees, and Divergence Times. Mol. Biol. Evol 34, 1812–1819. [PubMed: 28387841]

Letunic I, and Bork P (2016). Interactive tree of life (iTOL) v3: an online tool for the display and annotation of phylogenetic and other trees. Nucleic Acids Res 44, W242–W245. [PubMed: 27095192]

Li JS, Miralles Fusté J, Simavorian T, Bartocci C, Tsai J, Karlseder J, and Lazzerini Denchi E (2017). TZAP: A telomere-associated protein involved in telomere length control. Science 355, 638–641. [PubMed: 28082411]

Lord CJ, and Ashworth A (2017). PARP inhibitors: Synthetic lethality in the clinic. Science 355, 1152–1158. [PubMed: 28302823]

Manis JP, Morales JC, Xia Z, Kutok JL, Alt FW, and Carpenter PB (2004). 53BP1 links DNA damage-response pathways to immunoglobulin heavy chain class-switch recombination. Nat. Immunol 5, 481–487. [PubMed: 15077110]

Mi H, Huang X, Muruganujan A, Tang H, Mills C, Kang D, and Thomas PD (2017). PANTHER version 11: expanded annotation data from Gene Ontology and Reactome pathways, and data analysis tool enhancements. Nucleic Acids Res 45, D183–D189. [PubMed: 27899595]

Nakamura M, Kondo S, Sugai M, Nazarea M, Imamura S, and Honjo T (1996). High frequency class switching of an IgM+ B lymphoma clone CH12F3 to IgA+ cells. Int. Immunol 8, 193–201. [PubMed: 8671604]

Ochs F, Somyajit K, Altmeyer M, Rask MB, Lukas J, and Lukas C (2016). 53BP1 fosters fidelity of homology-directed DNA repair. Nat. Struct. Mol. Biol 23, 714–721. [PubMed: 27348077]

Pageau GJ, and Lawrence JB (2006). BRCA1 foci in normal S-phase nuclei are linked to interphase centromeres and replication of pericentric heterochromatin. J. Cell Biol 175, 693–701. [PubMed: 17145961]

Palm W, and de Lange T (2008). How shelterin protects mammalian telomeres. Annu. Rev. Genet 42, 301–334. [PubMed: 18680434]

Rappold I, Iwabuchi K, Date T, and Chen J (2001). Tumor suppressor p53 binding protein 1 (53BP1) is involved in DNA damage-signaling pathways. J. Cell Biol 153, 613–620. [PubMed: 11331310]

Räschle M, Smeenk G, Hansen RK, Temu T, Oka Y, Hein MY, Nagaraj N, Long DT, Walter JC, Hofmann K, et al. (2015). DNA repair. Proteomics reveals dynamic assembly of repair complexes during bypass of DNA cross-links. Science 348, 1253671. [PubMed: 25931565]

Rhee HW, Zou P, Udeshi ND, Martell JD, Mootha VK, Carr SA, and Ting AY (2013). Proteomic mapping of mitochondria in living cells via spatially restricted enzymatic tagging. Science 339, 1328–1331. [PubMed: 23371551]

Savage KI, and Harkin DP (2015). BRCA1, a 'complex' protein involved in the maintenance of genomic stability. FEBS J 282, 630–646. [PubMed: 25400280]

Schultz LB, Chehab NH, Malikzay A, and Halazonetis TD (2000). p53 binding protein 1 (53BP1) is an early participant in the cellular response to DNA double-strand breaks. J. Cell Biol 151, 1381–1390. [PubMed: 11134068]

Shannon P, Markiel A, Ozier O, Baliga NS, Wang JT, Ramage D, Amin N, Schwikowski B, and Ideker T (2003). Genome Res 13, 2498–2504. [PubMed: 14597658]

Sonnhammer EL, and Östlund G (2015). InParanoid 8: orthology analysis between 273 proteomes, mostly eukaryotic. Nucleic Acids Res 43, D234–D239. [PubMed: 25429972]

Suzuki K, Bose P, Leong-Quong RY, Fujita DJ, and Riabowol K (2010). REAP: A two minute cell fractionation method. BMC Res. Notes 3, 294. [PubMed: 21067583]

Toledo LI, Altmeyer M, Rask MB, Lukas C, Larsen DH, Povlsen LK, Bekker-Jensen S, Mailand N, Bartek J, and Lukas J (2013). ATR prohibits replication catastrophe by preventing global exhaustion of RPA. Cell 155, 1088–1103. [PubMed: 24267891]

UniProt Consortium T (2017). UniProt: the universal protein knowledgebase. Nucleic Acids Res 45, 2699.

Viechtbauer W (2010). Conducting Meta-Analyses in R with the metafor Package. J. Stat. Soft 36.

Vizcaíno JA, Csordas A, Del-Toro N, Dianes JA, Griss J, Lavidas I, Mayer G, Perez-Riverol Y, Reisinger F, Ternent T, et al. (2016). 2016 update of the PRIDE database and its related tools. Nucleic Acids Res 44, 11033. [PubMed: 27683222]

Ward IM, Reina-San-Martin B, Olaru A, Minn K, Tamada K, Lau JS, Cascalho M, Chen L, Nussenzweig A, Livak F, et al. (2004). 53BP1 is required for class switch recombination. J. Cell Biol 165, 459–464. [PubMed: 15159415]

Wickham H (2009). ggplot2: Elegant Graphics for Data Analysis (Springer-Verlag).

Wu P, Takai H, and de Lange T (2012). Telomeric 3′ overhangs derive from resection by Exo1 and Apollo and fill-in by POT1b-associated CST. Cell 150, 39–52. [PubMed: 22748632]

Wyatt HD, Laister RC, Martin SR, Arrowsmith CH, and West SC (2017). The SMX DNA Repair Tri-nuclease. Molecular. cell 65, 848–860 e811. [PubMed: 28257701]

Xie X, Hu H, Tong X, Li L, Liu X, Chen M, Yuan H, Xie X, Li Q, Zhang Y, et al. (2018). The mTOR-S6K pathway links growth signalling to DNA damage response by targeting RNF168. Nat. Cell Biol 20, 320–331. [PubMed: 29403037]

Xu G, Chapman JR, Brandsma I, Yuan J, Mistrik M, Bouwman P, Bartkova J, Gogola E, Warmerdam D, Barazas M, et al. (2015). REV7 counteracts DNA double-strand break resection and affects PARP inhibition. Nature 521, 541–544. [PubMed: 25799992]

Zhu C, Lee V, Finn A, Senger K, Zarrin AA, Du Pasquier L, and Hsu E (2012). Origin of immunoglobulin isotype switching. Curr. Biol 22, 872–880. [PubMed: 22542103]

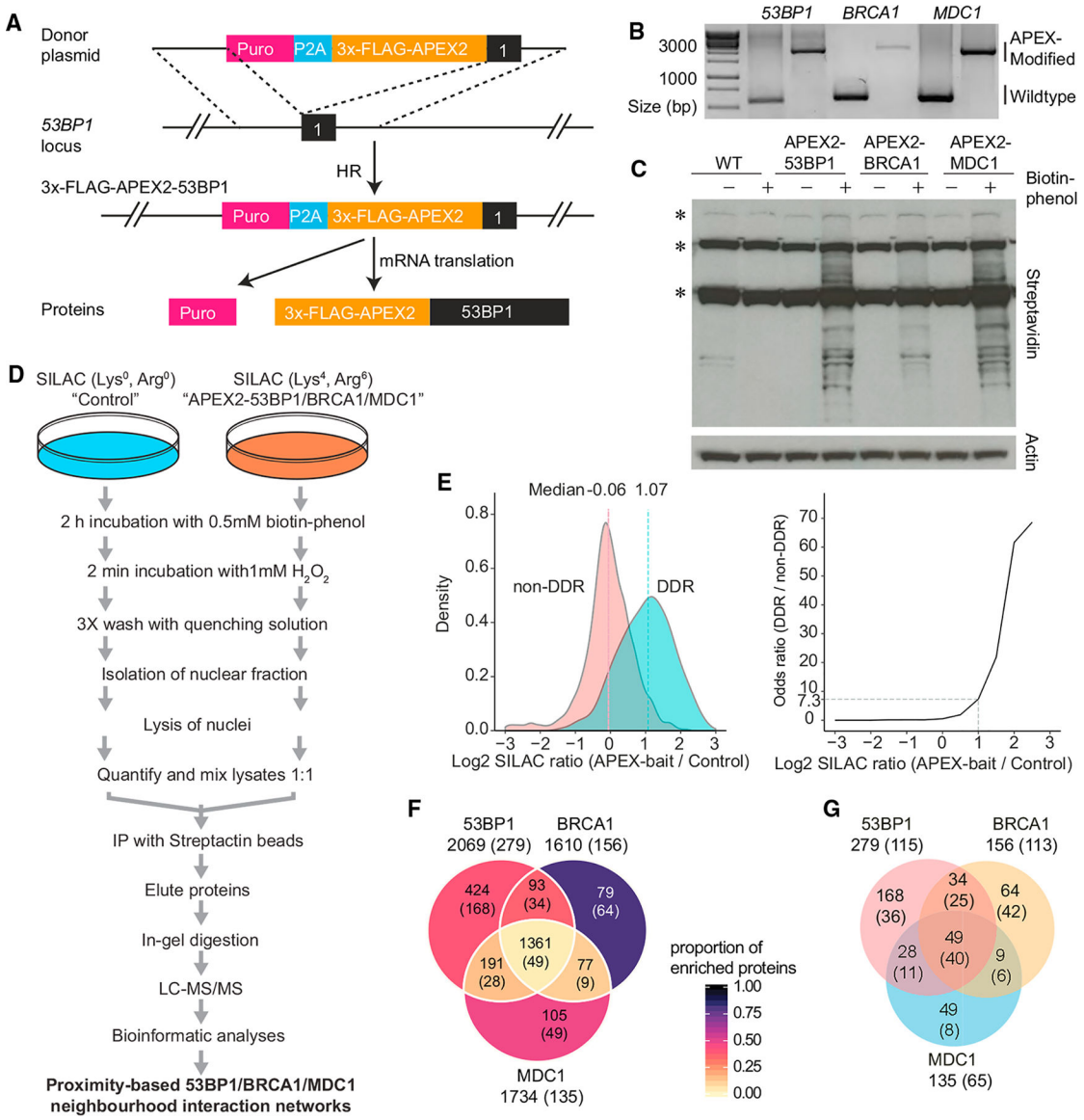

Figure 1. PROX-NET Analyses of the Endogenous 53BP1, BRCA1, and MDC1

(A) Strategy for CRISPR-based 33-FLAG-APEX2 tagging, exemplified by *53BP1*.

(B) Genomic confirmation of the APEX-modified *53BP1*, *BRCA1*, and *MDC1*.

(C) Confirmation of the APEX functionality by selective protein biotinylation in the APEX-engineered cells. The discrete bands, denoted with asterisks, show APEX-independent biotinylation by native enzymes.

(D) SILAC-based PROX-NET strategy for mapping the neighborhood interaction networks of APEX-tagged 53BP1, BRCA1, and MDC1.

(E) Distribution of SILAC ratios of known DDR and non-DDR factors quantified in the PROX-NET analyses. Median log2 SILAC ratios of each group are shown on the top of each distribution. The line plot (the right panel) shows the relationship between log2 SILAC ratio of quantified proteins and odds ratio of enrichment of known DDR factors.

(F) The overlap of all quantified, and significantly enriched proteins, among three baits. The numbers of quantified proteins are indicated without parentheses, and the numbers of significantly enriched proteins are indicated within parentheses. The color code in each area shows the fraction of the significantly enriched proteins (i.e., number of significantly enriched proteins/total number of proteins quantified).

(G) Overlap of the significantly enriched proteins among different baits. The Venn diagram shows the number of proteins enriched in PROX-NET analysis of each bait and their overlap with the other baits. The numbers in parentheses indicate the numbers of known DDR factors enriched in the dataset.

See also Figures S1 and S2 and Table S1.

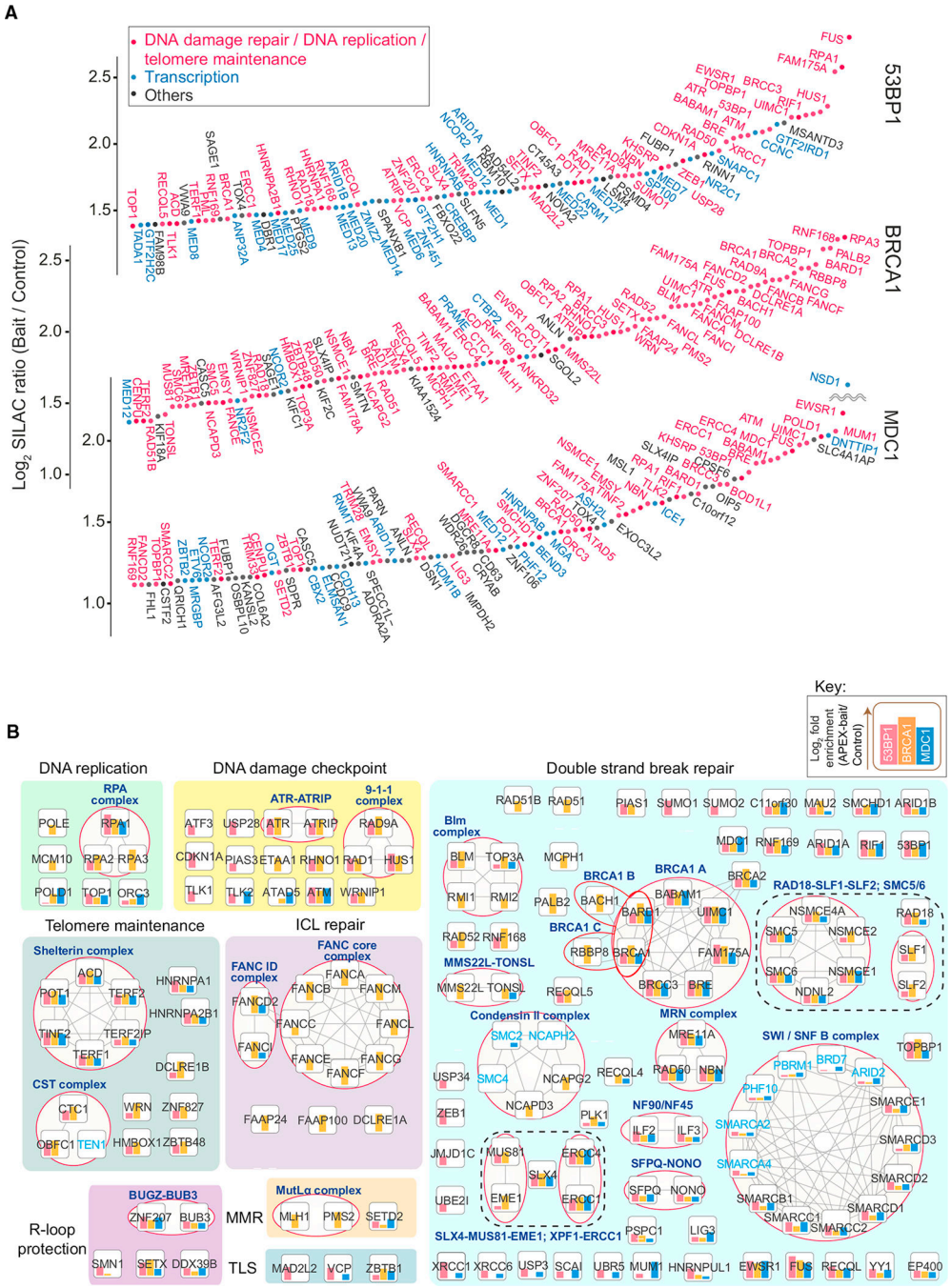

Figure 2. The Landscape of 53BP1, BRCA1, and MDC1 Interaction Neighborhoods

(A) The rank plot of 100 most highly enriched proteins in proximity to 53BP1, BRCA1, and MDC1. The proteins above the line were commonly enriched in at least two baits, whereas the proteins below the line were specifically enriched with the indicated baits.

(B) Proteins enriched in PROX-NET analyses are grouped according to their role in specific pathways, and known protein complexes and interactions are shown. Protein complexes are circled red, larger protein assemblies are indicated with dotted lines, and names of protein complexes are indicated in bold, dark blue text. Protein complex members that were not

enriched significantly, or were not identified, are indicated in light blue text. The red, orange, and blue bars above each protein show the bait specificity and degree of enrichment. See also Figures S1, S2, and S3 and Tables S2 and S3.

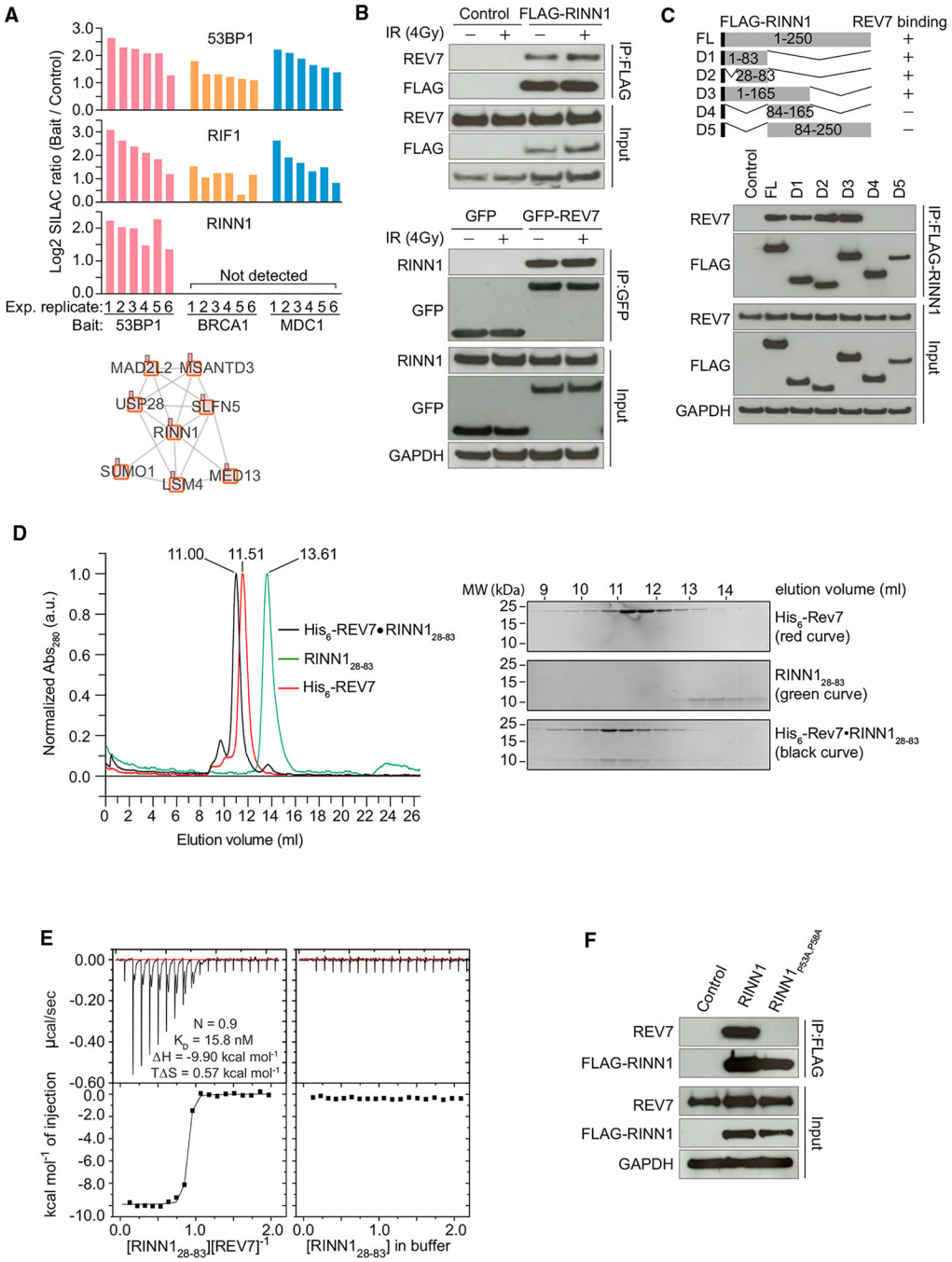

Figure 3. RINN1 Directly Interacts with REV7

(A) The bar chart shows log2 fold enrichment of 53BP1, RIF1, and RINN1 in PROX-NET dataset of 53BP1, BRCA1, and MDC1. The network shows *de novo* predicted interactions of RINN1.

(B) Reciprocal interaction between RINN1 and REV7. FLAG-RINN1 and GFP-REV7 were immunoprecipitated, and interaction with the endogenous REV7 and RINN1, respectively, was analyzed by immunoblotting.

(C) Mapping of REV7 interacting region in RINN1.

(D) The elution profiles (the top panel) of recombinant His_6-$REV7_{R124A}$ and $RINN1_{28–83}$ and His_6-REV7·$RINN1_{28–83}$ in a S75 10/300 analytical size exclusion chromatography (SEC) column. Fractions from analytical SEC runs were analyzed by SDS-PAGE and Coomassie staining for the whole elution range, showing elution of the REV7·$RINN1_{28–83}$ complex.

(E) Thermodynamic analysis of the $REV7_{R124A}$-$RINN1_{28–83}$ interaction (left panel). $REV7_{R124A}$ binds tightly to $RINN1_{28–83}$ with a nanomolar affinity (K_D = 15.8 nM). The control (the right panel) shows titration of $RINN1_{28–83}$ in buffer alone.

(F) Mutation of conserved P53 and P58 abolishes RINN1 interaction with REV7.

See also Figure S4 and Table S4.

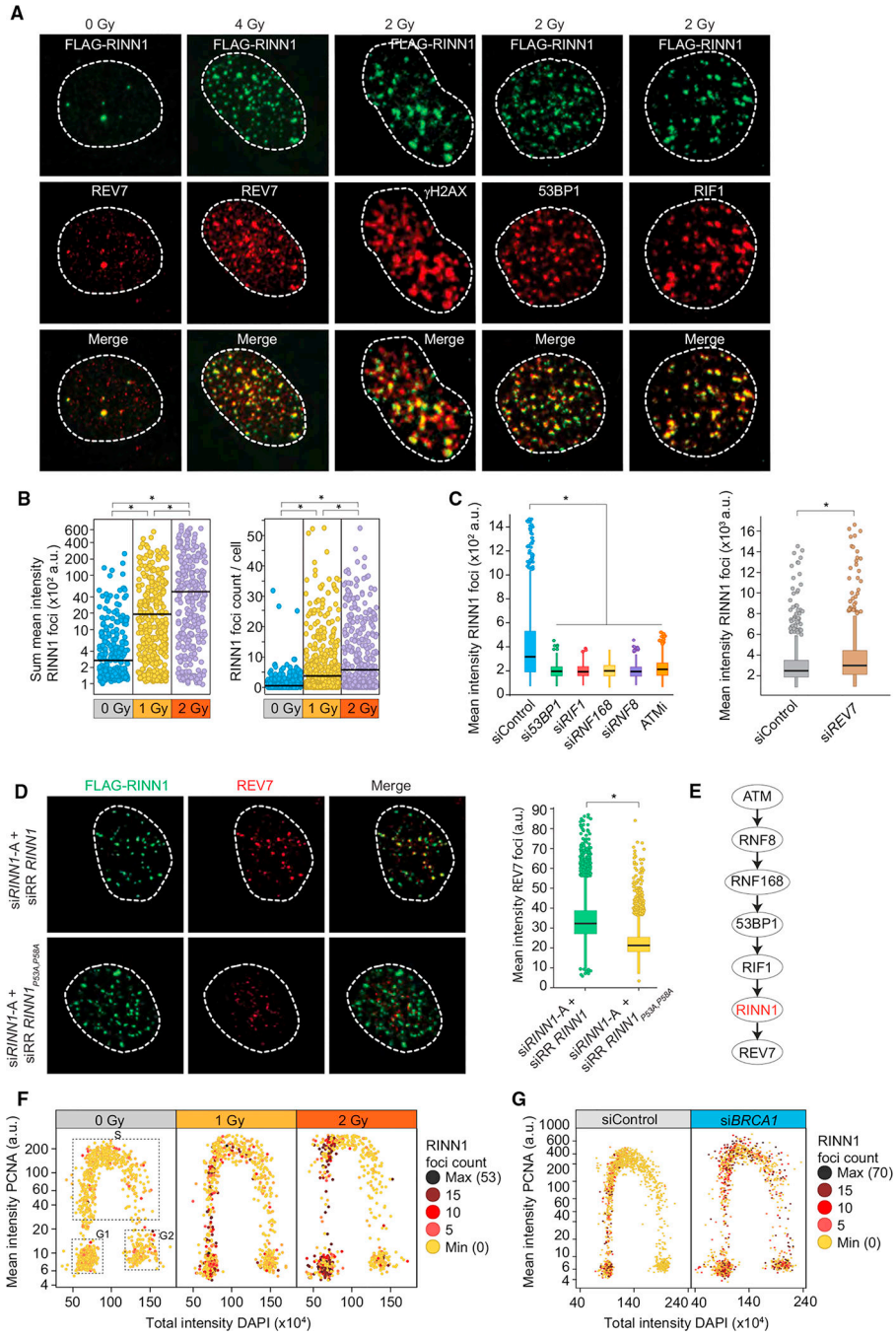

Figure 4. RINN1 Is Recruited to DSBs through the ATM-RNF8-RNF168–53BP1-RIF1 Axis, and the Recruitment Is Regulated by BRCA1 during the Cell Cycle

(A) RINN1 recruitment to IRIF and co-localization with γH2AX, REV7, 53BP1, and RIF1.

(B) Quantification of RINN1 IRIF count and intensity without or with the indicated doses of IR. RINN1 IRIFs were quantified at a single-cell level using quantitative image-based cytometry (QIBC) (Toledo et al., 2013). a.u., arbitrary units. *p < 0.05, approximative Wilcoxon-Mann-Whitney test.

(C) RINN1 recruitment to IRIF requires the ATM-RNF8-RNF168–53BP1-RIF1 axis, but not REV7; quantification as in (B). *p < 0.05, approximative Wilcoxon-Mann-Whitney test. (IR: 2Gy, 1-hr recovery).

(D) Expression of siRNA-resistant *RINN1* wild-type, but not $RINN1_{P53A,P58A}$, restores REV7 recruitment to IRIF in cells depleted of the endogenous *RINN1*. Representative images and quantification (the bar chart) of REV7 foci intensity are shown. (IR: 4Gy, 1-hr recovery). *p < 0.05, approximative Wilcoxon-Mann-Whitney test.

(E) Pathway diagram for the recruitment of RINN1 to DNA damage sites.

(F) QIBC-based quantification of RINN1 foci intensity in individual cells during the cell cycle. Cells were left untreated or were exposed to ionization radiation (1 Gy or 2 Gy, 1-hr recovery).

(G) RINN1 recruitment to IRIF in control and *BRCA1*-depleted cells during the cell cycle. (IR: 2Gy, 1-hr recovery).

See also Figures S5 and S6.

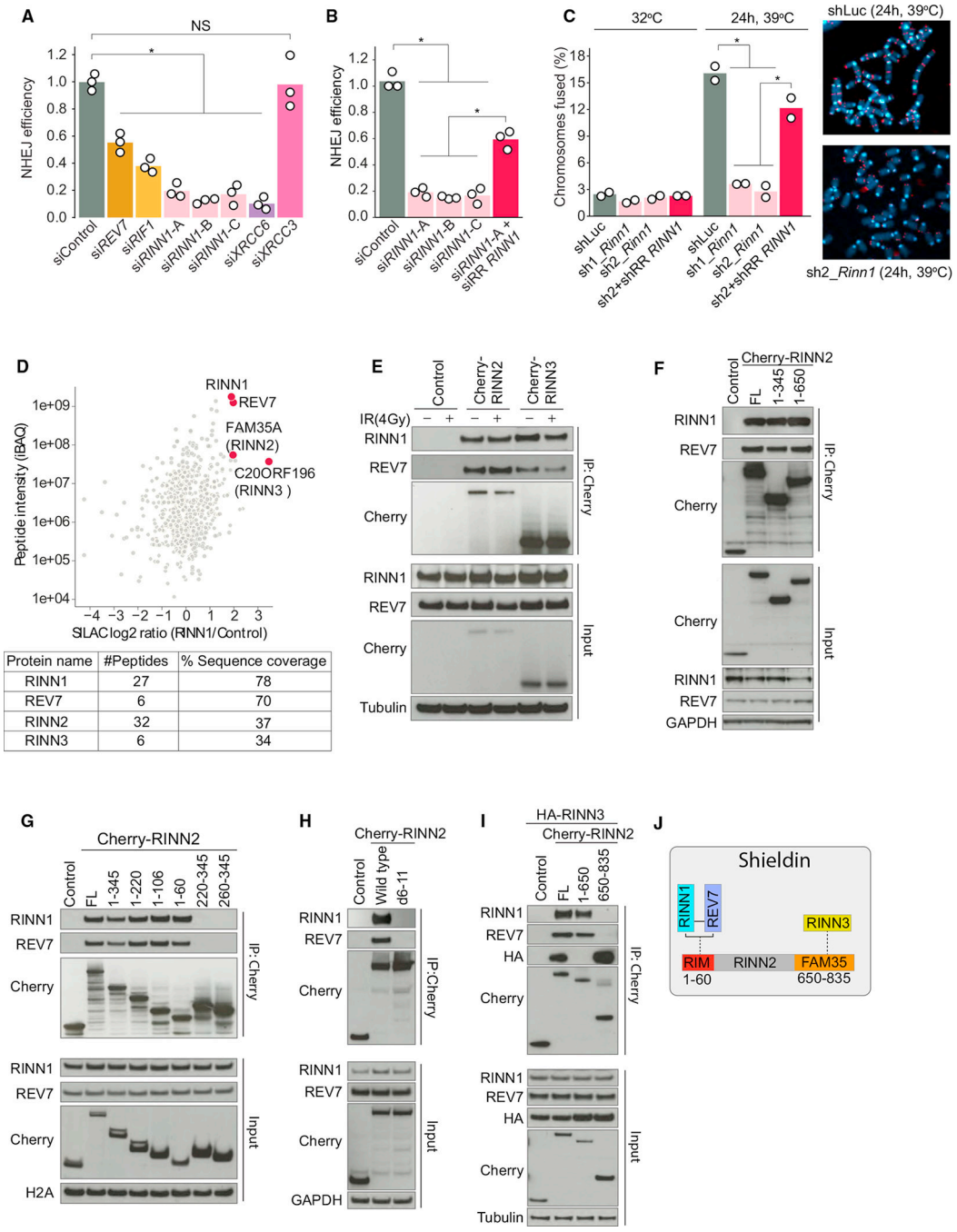

Protein name	#Peptides	% Sequence coverage
RINN1	27	78
REV7	6	70
RINN2	32	37
RINN3	6	34

Figure 5. RINN1 Regulates NHEJ and Forms the Novel Shieldin Complex with REV7 and RINN2–3

(A) NHEJ efficiency (relative to control) was quantified using the EJ5-GFP reporter after knockdown of the indicated genes. The bars show mean values, and circles indicate values from replicate experiments. *$p < 0.05$, Student's t test. NS, non-significant

(B) NHEJ-dependent repair was quantified using the EJ5-GFP reporter after transfection of the indicated RINN1 siRNAs and plasmids encoding siRNA-resistant RINN1 wild-type or $RINN1_{P53A,P58A}$; quantification as in (A). *$p < 0.05$, Student's t test.

(C) Telomere fusion in TRF2ts MEFs after knockdown of *Rinn1* and after the introduction of shRNA-resistant *RINN1* in the knockdown cells. (n = 2, with an >2,500 chromosome count). Representative images of metaphase spreads of control and *RINN1* shRNA-transduced TRF2ts MEFs; telomere FISH images were taken after 24 hr at 39°C. Telomeres and DNA are stained with PNA probe (red) and DAPI (blue), respectively. *$p < 0.05$, Cochran-Mantel-Haenszel test.

(D) Identification RINN1-interacting proteins by AP-MS. The scatterplot shows distribution of log2 SILAC ratio in RINN1-expressing cells as compared to control pull-down. The enriched bait protein and co-enriched shieldin components are marked with red dots, and protein names are indicated. The table shows the number of unique peptides and sequence coverage of the identified shieldin components.

(E–I) Validation of RINN2–3 interaction with RINN1 and REV7 (E), mapping of RINN1-REV7 interaction region in RINN2 (F–H), and mapping of the RINN3 binding region in RINN2 (I).

(J) A schematic representation of interactions among RINN1–3 and REV7. The RIM motif (RINN1-REV7 interaction motif) and FAM35 domain in RINN2 are indicated.

See also Figure S6 and Tables S5 and S6.

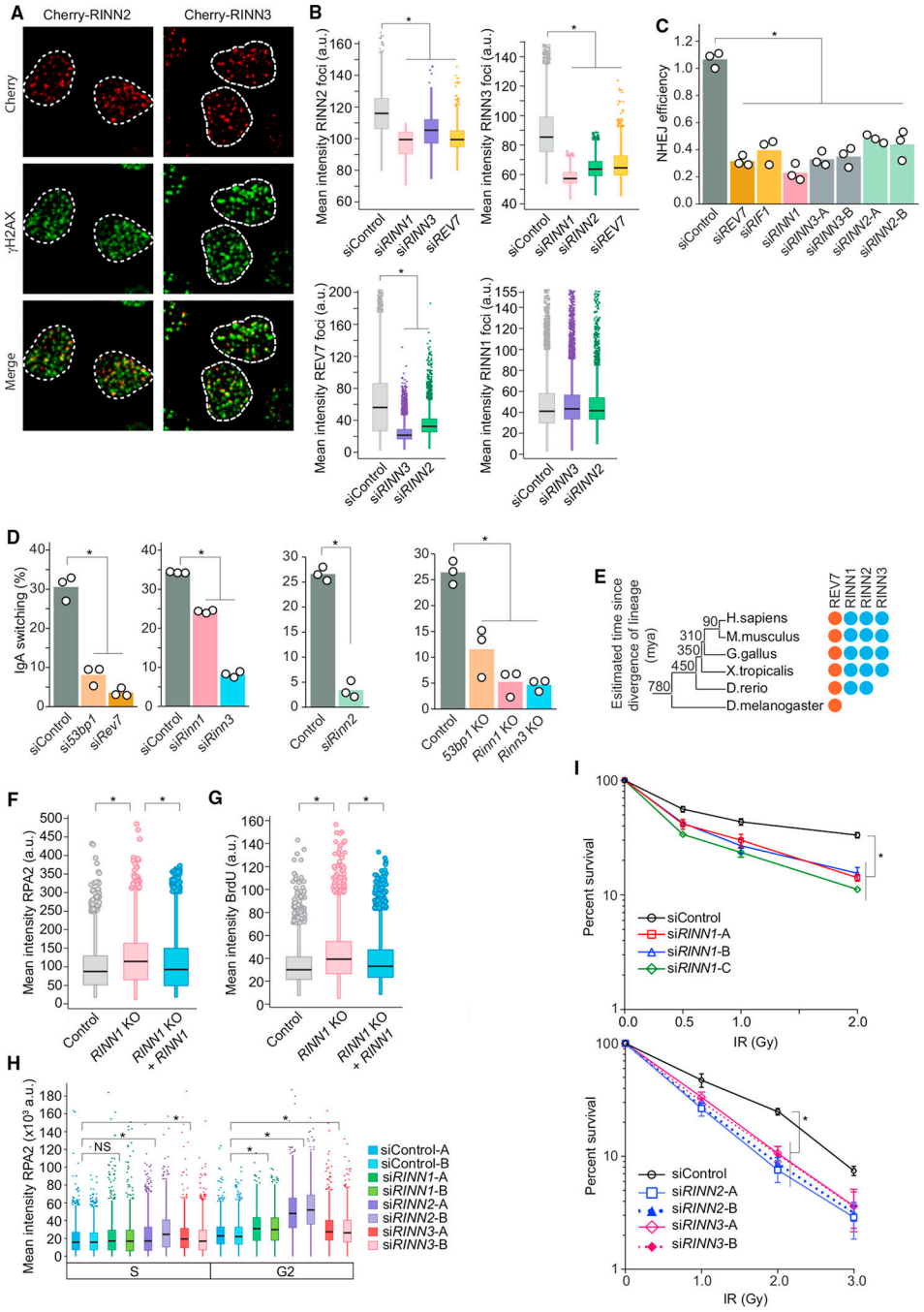

Figure 6. Higher Vertebrate-Specific Shieldin Is a Novel Regulator of NHEJ and DNA End Resection

(A) RINN2–3 localize to IRIF (IR: 4Gy, 2-hr recovery).

(B) Quantification of RINN1–3 and REV7 recruitment to IRIF in cells depleted of the indicated genes. (IR: 4Gy, 2-hr recovery). *p < 0.05, approximative Wilcoxon-Mann-Whitney test.

(C) Depletion of *RINN2–3* impairs NHEJ, assay done as in Figure 5A. *p < 0.05, Student's t test.

(D) Genetic deletion or knockdown of *Rinn1–3* impairs immunoglobulin CSR in CH12 cells. *53bp1* and *Rev7* serve as control. The indicated genes were deleted using the CRISPR technology or were depleted using siRNA. *p < 0.05, Student's t test.

(E) Phylogenic relationship and conservation of the member of the shieldin complex. The number at each branch point indicates the estimated divergent time. mya, million years ago.

(F) Quantification of chromatin binding of RPA2 in IR-treated (4Gy, 2-hr recovery) *RINN1* knockout U2OS cells and the knockout cells reconstituted with *RINN1*. *p < 0.05, approximative Wilcoxon-Mann-Whitney test.

(G) Quantification of native BrdU staining in control and *RINN1* knockout U2OS cells. (IR: 2Gy, 4-hr recovery). *p < 0.05, approximative Wilcoxon-Mann-Whitney test.

(H) Quantification of chromatin binding of RPA2 in IR-treated (4Gy, 2-hr recovery) cells after knockdown of the indicated genes. *p < 0.05, approximative Wilcoxon-Mann-Whitney test. NS, non-significant.

(I) Clonogenic survival of U2OS cells after exposure to ionizing radiation. Control and *RINN1–3* depleted cells were exposed to the indicated doses of ionization radiation and the numbers of surviving colonies were counted on day 9. Error bars represent standard error of mean. *p < 0.05, Student's t test.

See also Figures S6 and S7.

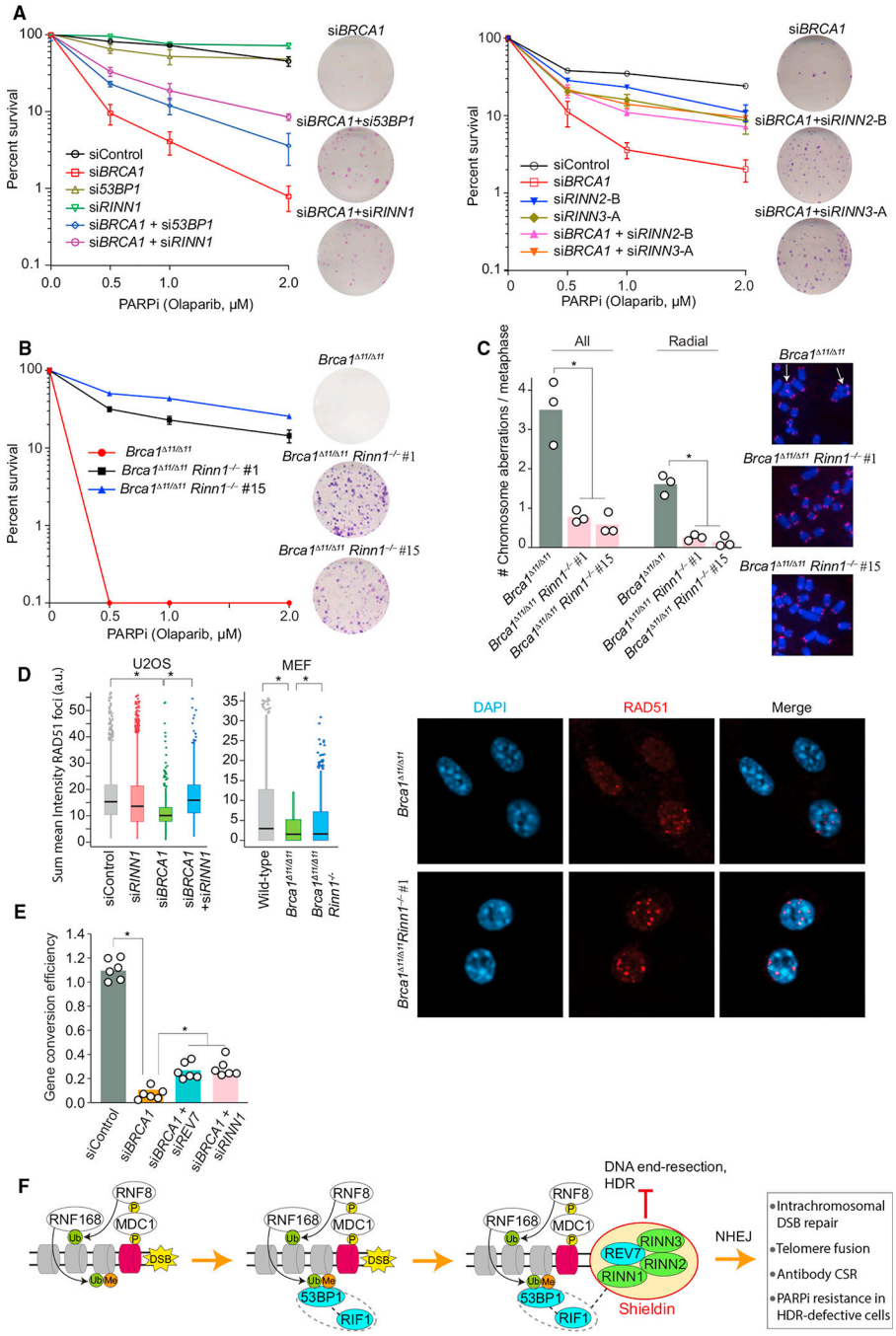

Figure 7. Shieldin Impacts PARP Inhibitor Sensitivity and HDR in *BRCA1*-Depleted Cells

(A) Quantification of long-term survival of control and olaparib-treated U2OS cells in clonogenic assays. The representative images show crystal violet-stained colonies of olaparib-treated (0.5 μM) cells. 48 hr after transfection of the indicated siRNAs, cells were treated with the specified concentrations of olaparib, and the colonies were counted on day 9. Error bars represent standard error of mean.

(B) Clonogenic survival of *Brca1*$^{\Delta 11/\Delta 11}$ and *Brca1*$^{\Delta 11/\Delta 11}$*Rinn1*$^{-/-}$ cells after treatment with the indicated concentrations of olaparib. Error bars represent standard error of mean.

(C) Frequency of chromosomal abnormalities and formation of radial chromosomes in *Brca1*$^{\Delta 11/\Delta 11}$ and *Brca1*$^{\Delta 11/\Delta 11}$*Rinn1*$^{-/-}$ cells after treatment with olaparib (1 μM). Representative images of metaphase spreads derived from the indicated MEFs. Telomeric PNA probe (red) and DAPI (blue). Arrows point to representative radial chromosomes. *$p < 0.05$, Student's t test.

(D) Quantification of RAD51 foci intensity in U2OS cells depleted of *RINN1* and/or *BRCA1* (the left panel), as well as in *Brca1*$^{\Delta 11/\Delta 11}$ and *Brca1*$^{\Delta 11/\Delta 11}$*Rinn1*$^{-/-}$ MEFs (the right panel). Representative images show RAD51 foci in *Brca1*$^{\Delta 11/\Delta 11}$ and *Brca1*$^{\Delta 11/\Delta 11}$*Rinn1*$^{-/-}$ cells. (IR: 2Gy, 2-hr recovery). *$p < 0.05$, approximative Wilcoxon-Mann-Whitney test.

(E) Knockdown of *RINN1* partially restores GC efficiency in *BRCA1*-depleted cells; *REV7* knockdown serves as a positive control. *$p < 0.05$, Student's t test.

(F) Proposed model of shieldin function in DSB repair. 53BP1-specific pathway components are depicted with solid color background, proteins in cyan indicate previously known 53BP1 pathway components, and proteins in green indicate the pathway components identified in this work.

See also Figure S7.

KEY RESOURCES TABLE

REAGENT or RESOURCE	SOURCE	IDENTIFIER
Antibodies		
Sheep polyclonal RINN1	This paper	N/A
Rabbit monoclonal REV7	Abcam	Cat#ab180579
Mouse monoclonal FLAG	Sigma	Cat#F1804-200UG
Rabbit polyclonal 53BP1	Santa Cruz	Cat#sc22760
Mouse monoclonal 53BP1	Merck Millipore	Cat# MAB3802
Rabbit polyclonal RAD51	BioAcademia	Cat#70-002
Human PCNA	Immuno concepts	Cat#2037
Mouse monoclonal BRCA1	Santa Cruz	Cat#sc6954
Mouse monoclonal Phospho-H2A.X S139 (clone JBW301)	Merck Millipore	Cat#05-636
Mouse monoclonal Phospho H2A.X S139	Biolegend	Cat#613401
Rabbit monoclonal Phospho H2A.X S139	Cell Signaling Technology	Cat#9718
Rabbit polyclonal GAPDH	Merck Millipore	Cat#ABS16
Mouse Monoclonal β-Actin	Sigma	A2228
Rabbit monoclonal RPA1	Abcam	Cat#ab79398
Rabbit polyclonal Cyclin A	Santa Cruz	Cat#sc751
Rabbit monoclonal Cyclin E	Abcam	Cat#ab33911
Mouse monoclonal BrdU	BD Bisciences	Cat#347580
Rabbit polyclonal H3 pSer10	Abcam	Cat#ab5176
Goat anti-Mouse polyclonal Alexa Fluor 488 conjugated Secondary antibody	ThermoFisher Scientific	Cat#A11029
Goat anti-Rabbit polyclonal Alexa Fluor 488 conjugated Secondary antibody	ThermoFisher Scientific	Cat#A11034
Goat anti-Mouse polyclonal Alexa Fluor 568 conjugated Secondary antibody	ThermoFisher Scientific	Cat#A11031
Goat anti-Rabbit Alexa Fluor 568 conjugated Secondary antibody	ThermoFisher Scientific	Cat#A11036
Donkey anti-Sheep Alexa Fluor 568 conjugated Secondary antibody	ThermoFisher Scientific	Cat#A21099
FITC Rat Anti-Mouse monoclonal IgM	BD PharMingen	Cat#553437
PE Goat Anti-Mouse polyclonal IgA	Southern Biotech	Cat#1040-09
Mouse monoclonal RPA2	Abcam	Cat#ab2175
Mouse monoclonal αTubulin	Cell Signaling	Cat#2144
Mouse monoclonal Histone H2A (L88A6)	Cell Signaling	Cat#3636
Rabbit polyclonal MDC1	Abcam	Cat#ab11171
Rabbit polyclonal RIF1	Bethyl Laboratories	Cat#A300-567A
Rabbit polyclonal H2A.X	Abcam	Cat#ab11175
Rabbit monoclonal Phospho-Chk1 (S345)	Cell Signaling Technology	Cat#2348
Mouse monoclonal ATM pS1981	Rockland	Cat#200-301-400
Mouse monoclonal RNF8 (B-2)	Santa Cruz	Cat#sc271462
Rabiit polyclonal RNF168	Merck Millipore	Cat#06-1130

REAGENT or RESOURCE	SOURCE	IDENTIFIER
Rabbit polyclonal mCherry	Abcam	ab167453
Mouse monoclonal HA-Tag (6E2)	Cell Signaling	Cat#2367
Bacterial and Virus Strains		
MAX Efficiency DH5α Competent Cells	ThermoFisher Scientific	Cat#18258-012
Chemicals, Peptides, and Recombinant Proteins		
BrdU Flow Kit	BD PharMingen	Cat#559619
EdU	Invitrogen	Cat#C10357
Lipofectamine 2000	Thermo Fisher Scientific	Cat#11668019
Lipofectamine RNAiMAX	Thermo Fisher Scientific	Cat#13778150
Lipofectamine LTX	Thermo Fisher Scientific	Cat#15338500
TRIzol	Thermo Fisher Scientific	Cat#15596-018
Trolox	Sigma	Cat#238813
KaryoMAX Colcemid Solution	Thermo Fisher Scientific	Cat#15210-040
TelC-Cy3 probe	Panagene	Cat#F1002
Pepsin	Sigma	Cat#10108057001
VECTASHIELD Mounting medium with DAPI	Vector Laboratories	Cat#H-1200
Olaparib	Selleck Chemicals	Cat#S1060
$RINN1_{28-83}$	This paper	N/A
$REV7_{R124A}$	This paper	N/A
CD40L	Peprotech	Cat#315-15
IL4	Sigma	Cat#11020
TGFβ	R&D systems	Cat#240-B-002
Deposited Data		
UniProtKB	UniProt Consortium, 2017	https://www.uniprot.org/uniprot/
TIMETREE	Kumar et. al, 2017	http://www.timetree.org/
PANTHER version 11	Mi et al., 2017	http://www.geneontology.org/page/go-enrichment-analysis
GTEx (2016-01-15_v7)	GTEx Consortium, 2013	https://www.gtexportal.org/home/
InParanoid (v8.0)	Sonnhammer and Östlund, 2015	http://inparanoid.sbc.su.se/cgi-bin/index.cgi
BioGrid (V3.4)	Chatr-Aryamontri et al., 2017	https://thebiogrid.org/
The MS raw data published in this study	Vizcaíno et al., 2016	PRIDE: PXD009284
Experimental Models: Cell Lines		
U2OS	ATCC	HTB-96
Jurkat	ATCC	TIB-152
CH12	Nakamura et al., 1996	N/A
HCT116	ATCC	CCL-247
SH-SY5Y	ATCC	CRL-2266
Kasumi-1	ATCC	CRL-2724
293FT	ThermoFisher Scientific	R70007
hTERT RPE-1	ATCC	CRL-4000
TRF2ts MEFs	Konishi and de Lange, 2008	N/A
Brca1$^{\Delta 11/\Delta 11}$ *MEFs*	Bunting et al., 2010	N/A

REAGENT or RESOURCE	SOURCE	IDENTIFIER
Brca1$^{\Delta 11/\Delta 11}$Rinn1$^{-/-}$ *MEFs*	This paper	N/A
Oligonucleotides		
Primer, siRNA, shRNA, and gRNA sequences	This paper	Table S7
Recombinant DNA		
List provided in Table S7	This paper	Table S7
Software and Algorithms		
MaxQuant	Cox et al., 2011	http://www.biochem.mpg.de/5111795/maxquant
R	N/A	https://www.r-project.org/
Cytoscape	Shannon et al., 2003	http://www.cytoscape.org/
ITOL	Letunic and Bork, 2016	https://itol.embl.de/
coin (1.2-2)	Hothorn et al., 2008	https://cran.r-project.org/web/packages/coin/coin.pdf
ggplot2 (2.2.1)	Wickham, 2009	https://cran.r-project.org/web/packages/ggplot2/ggplot2.pdf
metafor (0.5-4)	Viechtbauer, 2010	https://cran.r-project.org/web/packages/metafor/metafor.pdf
msa(1.10.0)	Bodenhofer et al., 2015	https://bioconductor.org/packages/release/bioc/vignettes/msa/inst/doc/msa.pdf
MCL(1.0)	N/A	https://cran.r-project.org/web/packages/MCL/MCL.pdf